A numerical estimate of the tidal energy in the Lofoten area

Master thesis in energy

Johannes Sandanger Dugstad

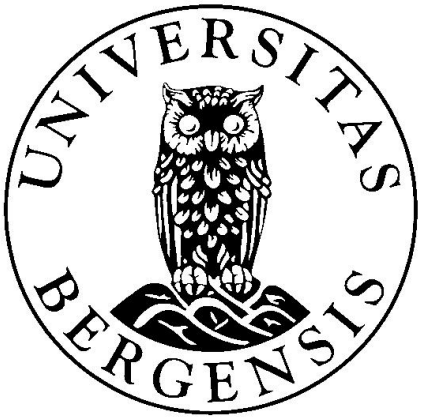

University of Bergen

Department of mathematics and geophysics

May 28, 2014

Acknowledgements

This master thesis is carried out as a part of the master program in energy at the mathematical and geophysical institute at the University of Bergen.

I will especially thank my supervisor Jarle Berntsen for all the help he has given me during this work. I am very thankful for all the advices he has given me. I appreciate all the discussions we have had when I have come by his office and asked for help. I will also like to thank Helge Avlesen for all his effort by setting up the model that I have used.

I will also thank my fellow students for being around during the last 5 years. All the lunches we have had together has been highly appreciated. As I now probably will leave the university, I will miss all the serious and sometimes very unserious conversations we have had during the years.

At last I will thank my family for all the support and motivation throughout the work.

Johannes S. Dugstad
Bergen May 2014

Abstract

In the following study the energy potential associated with tidal energy will be investigated. A depth integrated model based on the Navier Stokes equations and the continuity equation will be applied to simulate the tides around the Lofoten area in the northern Norway. The model applies a 250 m grid resolution. The only tidal component taken into consideration is the M_2-component.

In the study, computations of available potential and kinetic energy fluxes will be performed. It is computed a potential energy reservoir about 200 times larger than the kinetic energy for the Lofoten area. A substantial conversion of potential energy to kinetic energy occurs as the tide propagates from the deep ocean to the channels between the Lofoten islands. The Lofoten islands make a blocking effect which causes phase differences between the tide on the inside and the outside of the islands. The kinetic energy in the channels is estimated to 2.45 TWh. The potential energy in the channels is estimated to 72.9 TWh.

Contents

Chapter 1

Introduction

1.1 Tidal flow

The surface elevation of the ocean is affected by the tide. As the tide is created by the gravitational force from the moon and the sun, a wave called the Kelvin wave (The Kelvin wave will be explained later in this chapter) will start to propagate. This will make changes in the surface elevation. The changes in the surface elevation create the tidal currents. The currents will move the water from one place to another. The tide behaves periodically and one location experiences high tide and low tide approximately twice per day.

1.2 Tidal energy: Potential and kinetic

If the water has to take the way through a narrow channel, the velocity of the current will increase. This can make it possible to utilize the tidal energy. The kinetic energy is a measurement of how much energy that can be utilized from the current as it moves through the channel. The potential energy is a measurement of how much energy that is available based on the pressure differences due to the changes in the surface elevation between two points in the channel.

1.3 Dissipation of energy

The potential energy resources on the deep ocean are of great magnitude. However, some of it will dissipate due to factors such as bottom friction, viscosity and wind stress. In Egbert and Ray, see [7], it is stated that the estimated total amount of tidal energy that is dissipated during a year in the earth-moon-system is about 2.5 TW. For the earth-moon-sun-system this number is about 3,7 TW. This means that during a year there will dissipate

$3,7TW * 365 * 24h \approx 32000$ TWh. The energy consumption in the world in 2011 was about 143000 TWh, see Sælen [21], so we see that the dissipation is a very large number. If we were able to exploit this we would have a huge energy resource.

In the ocean, most of the energy dissipation is caused by the bottom boundary layer in shallow seas as stated in [7]. This suggests that most of this dissipation occurs near the land boundary in the shallow seas. The dissipation occurs directly because of friction but also because of mixing of water of different densities. When the tide propagates towards or along a land boundary, it will meet a sloping topography. This produces an internal wave at the interface between two layers of fluid with different densities. This wave has the same frequency as the surface tide. This is called an internal tide. As stated in Garrett and Kunze, see [10], the internal tides cause dramatic vertical displacements of density surfaces in the ocean interior. Water parcels with different densities will therefore start to do work on each other and this will lead to energy dissipation.

As already mentioned, most of the energy dissipation occurs near the land boundary. However, there is also some energy that dissipates in the deep ocean. It is stated in [7] that 1 TW of the dissipated energy occurs in the deep ocean. Mixing because of rough topography on the bottom can be one reason for this loss, but it is very difficult to quantify how much this will affect it.

1.4 The Kelvin wave

The moon and sun are the main causes of the tide. This will be discussed later in this chapter. When talking about the tide we are actually talking about a wave called the Kelvin wave. Kelvin waves are waves that require support by a lateral boundary. In this thesis this lateral boundary will be the Norwegian coast. On the northern hemisphere the Kelvin wave will always propagate with the coast on its right because of the Coriolis force. This explains why the Kelvin wave always will propagate northwards along the Norwegian coast and not southwards.

The Kelvin wave has phase speed $c = \sqrt{gH}$ where g is the gravity acceleration and H is the depth. The Kelvin wave in the North Sea comes in from the North of Scotland and propagates counterclockwise, see Gjevik [12]. This means it will propagate northwards with the west coast of Norway on its right. The tidal elevation increases as the wave propagates northwards. From the south of Lofoten to Vesterålen the elevation decreases. As the wave continues further north towards Finnmark, the surface elevation will again increase. Both the

location and size of the channels are very beneficial for Lofoten and Saltstraumen. The narrow channels make the velocity large. In general we know that the energy flux is proportional to the velocity cubed so we see that if we double the velocity we will get 8 times as much power.

1.5 Tidal power plants

Exploitation of tidal energy is an increasing research field. The first tidal power plant was built in 1960 on the estuary of the Rance river in Brittany, France. This works as a basin that is filled up as the tide increases. When the tide is decreasing again, there will be a height difference of about 8 meters between the water in the basin and the water outside. The water is then used to drive turbines. The power plant produces about 240 MW.

When there are channels with strong currents, an option to utilize the energy could be to place water mills directly into the current. This has been tested in several places. One of the places is Kvalsundet in Hammerfest. As stated in [12] the turbines are said to be able to produce about 300 kW each.

1.6 The tidal components

Chapter 8 in [12] describes how the tide is affected by several tidal components. The components represent oscillations which can either reinforce each other or weaken each other. The greatest contribution to the tide is the contribution from the moon. This contribution is referred to as the M_2-component. The index 2 tells that the component has a half-daily period. The period of this component is 12.42 hours which means that we will have high and low tide almost twice per day. The second component is the S_2-component which represents the contribution from the sun. The period is 12 hours. The sum of these two components will mainly decide how the tide behaves. However, there are other components that also have some impact. The two most important will be explained. The N_2-component is the change of distance between the earth and the moon. This has a period of 12.66 hours. When the moon is far away, the tidal range is smaller than when the moon is close to the earth. The last component is the K_1-component which is the declination of the moon and the sun compared to the earth. The index 1 tells that the component has a period of about one day. The period is 23.93 hours. Between two high tides the elevation can change. This is mainly because the moon and sun sometimes stand lower than the equator plane and sometimes higher than the equator plane.

Together, these four components can describe how the tide behaves. In addition to this we know that some places have larger tidal ranges than other. This can be due to the local topography. For instance in Bay of Fundy in Canada there can sometimes be tidal ranges of about 20 meters. This is because the tidal period sometimes can coincide with a local oscillation, for instance a seiche which is a standing wave(see Chapter 3). The two oscillations can reinforce each other and give large surface elevations. This will give the extreme tidal ranges.

1.7 The focus of this thesis

This thesis will investigate the tidal currents that are created in the channels in Lofoten and Saltstraumen. It will study the behavior of the tide in this area and how much kinetic and potential energy that are available in the Lofoten area.

1.7.1 Box models

A box model is a very simplified model that assumes that the area we are interested in can be divided into rectangular boxes which make the calculation much easier. Despite this simplification the model can still be quite realistic. The box model approach has been used for Saltstraumen. Saltstraumen is different than the other currents in Lofoten. While the channels in Lofoten are channels that connects two open seas, Saltstraumen is a channel that connects the open ocean with a fjord on the inside. The box model approach is therefore more suitable for Saltstraumen since the fjord inside is of a finite size. With open ocean on both sides of the channels, certain non-accurate boundary conditions have to be considered. These are conditions such as how much of the ocean on the outside that would have been affected by the current in the channels. When dealing with a fjord on the inside, these approximations are avoided. The results developed with the box model will be compared with the same results obtained from the other model used for this thesis, namely the modified version of the Bergen ocean model as discussed in the following subsection.

1.7.2 The Lofoten area

The calculation for the Lofoten area will be based on a mathematical model which is a modified version of the Bergen ocean model(BOM), see [4]. This model calculates the velocity field and surface elevation of the tide as the tide propagates from just south of Lofoten and further north to the north end of Lofoten. These calculations are based on the 2-D version of the Navier Stokes equations, called the shallow water equations. These equations are developed in Chapter 2.

In the thesis, the model will be applied to understand the behavior of the tide in the Lofoten area during a tidal cycle. The velocity field and the surface elevation will be used to investigate the kinetic and potential energy fluxes through the channels. Furthermore the distribution of energy for the whole Lofoten area will be studied. Energy losses due to frictional forces will also be considered.

Chapter 2

Equations and approximations for geophysical flows

To describe the motion of a fluid, two main equations are applied. These are the continuity equation and the Navier Stokes equation. The Navier Stokes equation is a vector equation which consists of three separate equations, one for each direction. In this chapter the shallow water equations will be developed. These are based on the Navier Stokes equation and the continuity equation. The shallow water equations are beneficial to describe geophysical flows over large areas where the horizontal scale is much larger than the vertical scale.

Conservation of mass can be expressed as

$$\frac{\partial \rho}{\partial t} + \nabla \cdot (\rho \mathbf{U}) = 0 \, . \tag{2.1}$$

This is called the continuity equation. Furthermore, if we apply Newtons second law to fluids, we get the Navier Stokes equation. For geophysical flows, rotation is important, and the equations can be written as

$$\frac{D\mathbf{U}}{Dt} = -\frac{1}{\rho}\nabla p - 2\boldsymbol{\Omega} \times \mathbf{U} + \mathbf{g} + \mathbf{F} \, . \tag{2.2}$$

Here ρ is the density, p is the pressure, $\mathbf{U} = [u, v, w]$ is the velocity field, $\mathbf{g}$ is the gravity, $\boldsymbol{\Omega}$ is the earth rotation, $\mathbf{F}$ are external forces and $\frac{D}{Dt} = \frac{\partial}{\partial t} + u\frac{\partial}{\partial x} + v\frac{\partial}{\partial v} + w\frac{\partial}{\partial z}$ is the total derivative. The term $2\boldsymbol{\Omega} \times \mathbf{U}$ is the Coriolis acceleration and the earth rotation vector can be written as $\boldsymbol{\Omega} = \Omega \cos(\phi)\mathbf{j} + \Omega \sin(\phi)\mathbf{k}$. The cross product in Equation (2.2) then becomes

$$2\boldsymbol{\Omega} \times \mathbf{U} \cong 2\Omega(w\cos(\phi) - v\sin(\phi))\mathbf{i} + 2\Omega u \sin(\phi)\mathbf{j} - 2\Omega u \cos(\phi)\mathbf{k} \, ,$$

where ϕ is the latitude, that is, $\phi = 0$ is on the equator and $\phi = \frac{\pi}{2}$ is on the north pole. Furthermore, $[\mathbf{i}, \mathbf{j}, \mathbf{k}]$ denote the unit vectors in the x, y and z-directions respectively. In the

term multiplied with $\mathbf{i}$ we use the condition $wcos(\phi) \ll vsin(\phi)$. This is because the thin sheet approximation, that the horizontal scale is much larger than the vertical scale, requires $w \ll v$ as discussed in Kundu et al. [16]. This gives the equation

$$2\mathbf{\Omega} \times \mathbf{U} \cong -2\Omega v \sin(\phi)\mathbf{i} + 2\Omega u \sin(\phi)\mathbf{j} - 2\Omega u \cos(\phi)\mathbf{k} \, .$$

We define the Coriolis parameter to be $f = 2\Omega sin(\phi)$ and the reciprocal Coriolis parameter to be $f_* = 2\Omega cos(\phi)$. Then we can write the Coriolis acceleration as $-fv\mathbf{i} + fu\mathbf{j} - f_* u\mathbf{k}$. In the vertical Navier Stokes equation, the reciprocal Coriolis parameter is usually very small compared to the other terms and can generally be neglected.

2.1 Underlying approximations

Since the study of hydrodynamics always has to deal with turbulence and fluctuations it is necessary to study the statistically averaged flow. Reynolds suggested that we can split a variable into a mean part $\bar{\mathbf{U}}$ and a fluctuation part $\mathbf{U_f}$ as $\mathbf{U} = \bar{\mathbf{U}} + \mathbf{U_f}$ as stated in [16]. The same splitting is applied to the pressure and the density. The mean part is found by integrating the values over a certain time period. From now on, the mean variables will be used and the bars will be dropped. Furthermore, it will be assumed that the pressure is hydrostatic, that is, the pressure at a given depth equals the weight of the fluid above. The Boussinesq approximation, which is explained below, will also be applied.

As stated in [16], the Boussinesq approximation states that the density can be split into a reference value ρ_0 and a perturbation $\rho'(x, y, z, t)$ such that the density changes for the fluid can be neglected except where ρ is multiplied by the gravity. Before applying the Boussinesq approximation on Equation (2.1) we notice that

$$\frac{\partial \rho}{\partial t} + \nabla \cdot (\rho \mathbf{U}) = \frac{D\rho}{Dt} + \rho(\nabla \cdot \mathbf{U}) \, . \tag{2.3}$$

Applying the Boussinesq approximation gives

$$\begin{aligned} \frac{D\rho}{Dt} + \rho(\nabla \cdot \mathbf{U}) &= 0 \\ \Rightarrow \frac{1}{\rho}\frac{D\rho'}{Dt} + \nabla \cdot \mathbf{U} &= 0 \, . \end{aligned} \tag{2.4}$$

The approximation suggests that the left term is very small compared to the right in the second line in Equation (2.4). This gives the incompressible form of the continuity equation.

$$\Rightarrow \nabla \cdot \mathbf{U} = \frac{\partial u}{\partial x} + \frac{\partial v}{\partial y} + \frac{\partial w}{\partial z} = 0 \, . \tag{2.5}$$

Thus the continuity equation states the conservation of volume as well as conservation of mass.

The momentum equation, (2.2) can be written on component form as also stated in Berntsen [4]. For the x and y-directions, ρ is only included in the pressure terms. According to the Boussinesq approximation ρ is displaced by ρ_0. In Cushman-Roisin and Beckers [6], a scaling analysis has been done to compare the typical magnitudes for the terms in the equation for the z-direction. This suggests that the dominating terms are the pressure and gravity terms. The result is the following system of equations.

$$\begin{aligned} \frac{\partial u}{\partial t} + \mathbf{U_H} \cdot \nabla u - fv &= -\frac{1}{\rho_0}\frac{\partial p}{\partial x} + F_x \ , \\ \frac{\partial v}{\partial t} + \mathbf{U_H} \cdot \nabla v + fu &= -\frac{1}{\rho_0}\frac{\partial p}{\partial y} + F_y \ , \\ \rho g &= -\frac{\partial p}{\partial z} \ . \end{aligned} \tag{2.6}$$

The velocity field $\mathbf{U_H}$ denotes the horizontal velocity field $\mathbf{U_H} = [u, v]$. See the beginning of the following section for the explanation why this has been applied. We also notice that for the equation in the z-direction we have the hydrostatic balance.

2.2 The shallow water equations

As already pointed out, for the development of the shallow water equations, a horizontal scale that is much larger than the vertical scale is assumed. When the wavelength is much larger than the depth of the flow, the vertical velocity is much smaller than the horizontal velocities. We therefore introduce the velocity field $\mathbf{U_H} = [u, v]$.

To develop the shallow water equations, we consider a homogeneous and non-stratified flow with layer thickness $h(x, y, t)$ and a reference height $H(x, y)$ from $z = 0$ to the mean surface level using positive z-direction upwards. The surface elevation is denoted by $\eta(x, y, t)$. This gives $h(x, y, t) = \eta(x, y, t) + H(x, y)$. The situation is depicted in Figure 2.1.

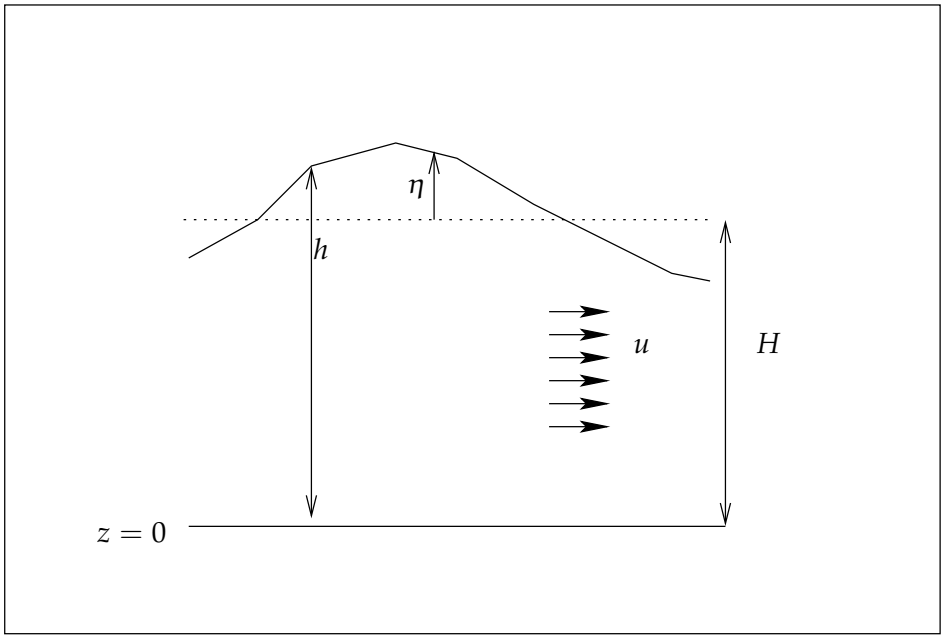

Figure 2.1: Diagram of the flow

From the previous section we have that the pressure is hydrostatic. This gives that the pressure at height z from the bottom can be written as $p = \rho_0 g(H + \eta - z)$. At the surface $z = H$ this gives $p(H) = \rho_0 g\eta$. This is the dynamic boundary condition. By substituting this expression for p, the horizontal pressure terms can be written as $\frac{\partial p}{\partial x} = \rho_0 g\frac{\partial \eta}{\partial x}$ and $\frac{\partial p}{\partial y} = \rho_0 g\frac{\partial \eta}{\partial y}$. Since η is independent of z, these expressions are independent of z, which means that the horizontal motion is also independent of z. Then we have that $\frac{\partial u}{\partial x}$ and $\frac{\partial v}{\partial y}$ are independent of z. It follows that w must vary linearly with z. Integrating Equation (2.5) across the water column, as discussed in [6] and [16] gives

$$(\frac{\partial u}{\partial x} + \frac{\partial v}{\partial y}) \int_0^h dz + [w]_0^h = 0 \, .$$

We apply the kinematic boundary condition that the flow cannot penetrate the bottom, which means that the velocity must be tangent to the land boundary, that is $w(0) = 0$. At the surface we require that the velocity of a fluid particle normal to the surface must be the same as the velocity of the surface itself, that is $\nabla(z - \eta) \cdot \mathbf{U_H} = \frac{\partial \eta}{\partial t}$. With these conditions and after some manipulation we get the depth integrated continuity equation.

$$\frac{\partial \eta}{\partial t} + \frac{\partial}{\partial x}(hu) + \frac{\partial}{\partial y}(hv) = 0 \, . \tag{2.7}$$

For the x and y-directions of the momentum equations we get the following:

$$\frac{\partial u}{\partial t} + \mathbf{U_H} \cdot \nabla u - fv = -g\frac{\partial \eta}{\partial x} + F_x \ , \tag{2.8}$$

and

$$\frac{\partial v}{\partial t} + \mathbf{U_H} \cdot \nabla v + fu = -g\frac{\partial \eta}{\partial y} + F_y \ . \tag{2.9}$$

Equation (2.7)-(2.9) are called the shallow water equations. The terms F_x and F_y are the terms treating the stress components, often referred to as the Reynolds stress. The stress components can be viscosity, bottom friction and wind stress. The model in this thesis will only take the bottom friction and the viscosity terms into account. They will be presented in Chapter 4.

2.3 Calculation of energy fluxes

The shallow water equations consist of three equations and three unknowns, namely $\mathbf{U_H} = [u, v]$ and η. These variables are useful when calculating energy fluxes. Suppose we have a flow through some cross section with area A. Then the force F against this cross section can be written as $F = pA$ where p is the pressure. Since we have assumed that the current does not propagate in z-direction, the pressure can be written according to Bernoullis equation, see [16], as

$$p = \frac{1}{2}\rho|\mathbf{U_H}|^2 \ . \tag{2.10}$$

Thus the force is expressed as $F = \frac{1}{2}\rho|\mathbf{U_H}|^2 A = \frac{1}{2}\rho|\mathbf{U_H}|^2 H ds$ where H is the depth and ds is some length element in the horizontal direction. The kinetic energy flux is force times velocity so it can be expressed as

$$E_K = \int \frac{1}{2}\rho H|\mathbf{U_H}|^3 ds \ . \tag{2.11}$$

The unit of E_K is W=Js^{-1} which is energy per time.

The velocity field and surface elevation are also used for the calculation of the potential energy flux. The expression for the potential energy flux uses the fact that the change of the potential energy in a grid cell is dependent of the rate of current that comes into and leaves the cell and also the change of surface elevation in the cell. According to Garrett, see [11], this can be expressed as $E_{PGRID} = \nabla \cdot (gH\eta\mathbf{U_H})$. Again assuming the flow is through a cross section area A, we get by integrating over A and taking the density into account, $E_P = \int \rho \nabla \cdot (gH\eta\mathbf{U_H}) dA$. By applying Gauss theorem this equation can be rewritten as

$$E_P = \int \rho g H \eta \mathbf{U_H} \cdot \mathbf{n} ds \ . \tag{2.12}$$

n is the normal of the cross section area A and ds is again a length element in the horizontal direction. The potential energy flux also has unit W=Js^{-1}.

The volume flux in a channel has been calculated according to the discrete formula

$$\sum H|\mathbf{U_H}|\Delta x \; . \tag{2.13}$$

This formula has units [m^{3}s^{-1}]. It states that the volume flux is the volume of water that flows through a transect during one second.

Chapter 3

A box model for inlets

In this chapter, the tidal flow in and out of a closed basin will be investigated using a simple box model. Even though the box model is very simplified, we can get useful information about the illustrated problem. We will consider the closed fjord configuration depicted in Figure 3.1:

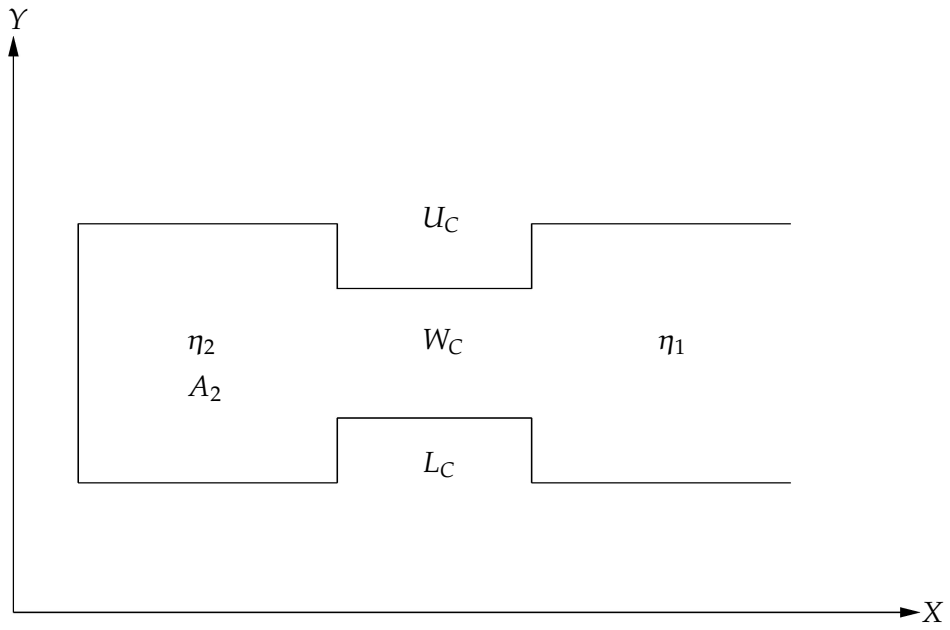

Figure 3.1: Example of a Box model situation

In the figure above, η_1 is the surface elevation in the open ocean outside the basin, η_2 is the surface elevation in the basin, U_C is the velocity of the current in the channel, W_C and L_C are the width and the length of the channel respectively, and A_2 is the surface area of the basin.

We use the initial conditions that U_C and η_2 are both zero at time $t = 0$. Further, we

will assume that the current only depends on the M_2-component. The tide is periodic so it is reasonable to assume that the incoming wave has a surface elevation that can be written as

$$\eta_1 = \eta_{M_2} \sin(\omega_{M_2} t) \, . \tag{3.1}$$

In Equation (3.1), η_{M_2} is the semi-diurnal tidal amplitude in meters while ω_{M_2} is the semi-diurnal tidal frequency in radians per sec.

3.1 Inlet with a linear drag coefficient

What follows in this section is also discussed in Eliassen [8]. We can assume that the surface elevation in the basin only will depend on the cross-section area of the channel, the velocity of the current through the channel and the surface area of the basin. Further, we assume that the change in velocity depends on the change of tidal elevation outside and inside the channel, the length of the channel and the gravity acceleration. If we assume the friction term is linear, we get the two following equations:

$$\begin{aligned} \frac{d\eta_2}{dt} &= -\frac{A_C U_C}{A_2} \, , \\ \frac{dU_C}{dt} &= g\frac{\eta_2 - \eta_1}{L_C} - RU_C \, . \end{aligned} \tag{3.2}$$

In Equation (3.2), A_C is the cross-section area in the channel, $A_C = W_C \times H_C$, where H_C is the depth of the channel and R is the friction drag with unit s^{-1}. These two equations can be solved numerically. Using the trapezoidal rule for the discretization of the equations, we get

$$\begin{aligned} \frac{\eta_2^{n+1} - \eta_2^n}{\Delta t} &= -\frac{A_C}{A_2}\frac{U_C^{n+1} + U_C^n}{2} \, , \\ \frac{U_C^{n+1} - U_C^n}{\Delta t} &= \frac{g}{2L_C}(\eta_2^{n+1} + \eta_2^n - (\eta_1^{n+1} + \eta_1^n)) - R\frac{U_C^{n+1} + U_C^n}{2} \end{aligned} \tag{3.3}$$

where U_C^{n+1} means the value of U_C at time step $n+1$. Solving these two equations for U_C^{n+1} and η_2^{n+1} we get the two equations on matrix form.

$$\begin{bmatrix} 1 & \frac{\Delta t A_C}{2A_2} \\ \frac{-g\Delta t}{2L_C} & \frac{1+R\Delta t}{2} \end{bmatrix} \begin{bmatrix} \eta_2^{n+1} \\ U_C^{n+1} \end{bmatrix} = \begin{bmatrix} \eta_2^n - \frac{\Delta t A_C}{2A_2} U_C^n \\ U_C^n(1 - \frac{R\Delta t}{2}) + \frac{g\Delta t}{2L_C}(\eta_2^n - (\eta_1^{n+1} + \eta_1^n)) \end{bmatrix} \, . \tag{3.4}$$

This system can be solved by Cramers rule, see [1], to get the values for the next time step.

To find the exact solution for the velocity field of this problem, we first take the time derivative of the second equation in (3.2) and then substitute the first one into the second one. This gives the second order differential equation

$$\frac{d^2U_c}{dt^2} + R\frac{dU_C}{dt} + QU_C = -Ecos(\omega_{M_2}t) \ . \tag{3.5}$$

The analytical solution of this equation is

$$U_C = Ae^{-k_1t} + Be^{-k_2t} + Ccos(\omega_{M_2}t) + Dsin(\omega_{M_2}t) \ . \tag{3.6}$$

The analytical solution of η_2 can be found by the second equation in (3.2). This gives

$$\begin{aligned} \eta_2 &= \frac{L_C}{g}\left[\frac{dU_C}{dt} + RU_C\right] + \eta_{M_2}\sin(\omega_{M_2}t) \\ \Rightarrow \eta_2 &= \frac{L_C}{g}\left[(-k_1A + RA)e^{-k_1t} + (-k_2B + RB)e^{-k_2t}\right] + \left[\frac{L_C}{g}(-C\omega_{M_2} + RD) + \eta_{M_2}\right]\sin(\omega_{M_2}t) \\ &\quad + \frac{L_C}{g}\left[\omega_{M_2}D + RC\right]\cos(\omega_{M_2}t) \ . \end{aligned} \tag{3.7}$$

The first two terms in Equation (3.6) and Equation (3.7) are called the transient terms. The constants being used in Equation (3.5)-(3.7) are given in Table 3.1

Q	=	$\frac{gA_C}{L_CA_2}$
E	=	$\frac{g}{L_C}\eta_{M_2}\omega_{M_2}$
k_1	=	$\frac{R-\theta}{2}$
k_2	=	$\frac{R+\theta}{2}$
θ	=	$\sqrt{R^2-4Q}$
D	=	$-\frac{R\omega_{M_2}}{R^2\omega^2_{M_2}+(Q-\omega^2_{M_2})^2}$
C	=	$\frac{E+DR\omega_{M_2}}{\omega^2_{M_2}-Q}$
B	=	$\frac{k_1C+D\omega_{M_2}}{k_2-k_1}$
A	=	$-C-B$

Table 3.1: The constants

The constants C and D are found by the method of undetermined coefficients, see Boyce and DiPrima [5], and the constants A and B are found by the initial conditions. Notice that the solutions of Equation (3.6) and Equation (3.7) show that the value of θ is real for this case.

When modeling the currents and surface elevations in Saltstraumen and Skjerstadfjorden, the approach given above may be applied. In Figure (3.1) we interpret the fjord with surface

elevation η_1 as Saltfjorden, the other fjord with surface elevation η_2 as Skjerstadfjorden and the channel that connects the two fjords as Saltstraumen. The constants used to calculate the values in Table 3.1 as given in [8] are the following:

η_{M_2}	=	0.869 m	Semi-diurnal tidal amplitude [m]
T_{M_2}	=	12.42h = 44712 s	Main semi-diurnal period [s]
ω_{M_2}	=	$\frac{2\pi}{T_{M_2}}$	Semi-diurnal tidal frequency [rad$\cdot$ s^{-1}]
W_C	=	333 m	Width of Saltstraumen [m]
H_C	=	15 m	Depth of Saltstraumen [m]
L_C	=	3330 m	Length of Saltstraumen [m]
A_C	=	$W_C \times H_C = 4995m^2$	Cross section area of Saltstraumen [m^2]
A_2	=	$2.16 * 10^8\ m^2$	Surface area of Skjerstadfjorden [m^2]
R	=	$6.9 \times 10^{-4}\ s^{-1}$	Drag coefficient [s^{-1}]

Table 3.2: Parameters for the Saltstraumen and Skjerstadfjorden box model

For these values the variable θ is real and the solution of the problem becomes as stated in Equation (3.6) and Equation (3.7). The surface elevations η_1 and η_2 are given over two tidal cycles:

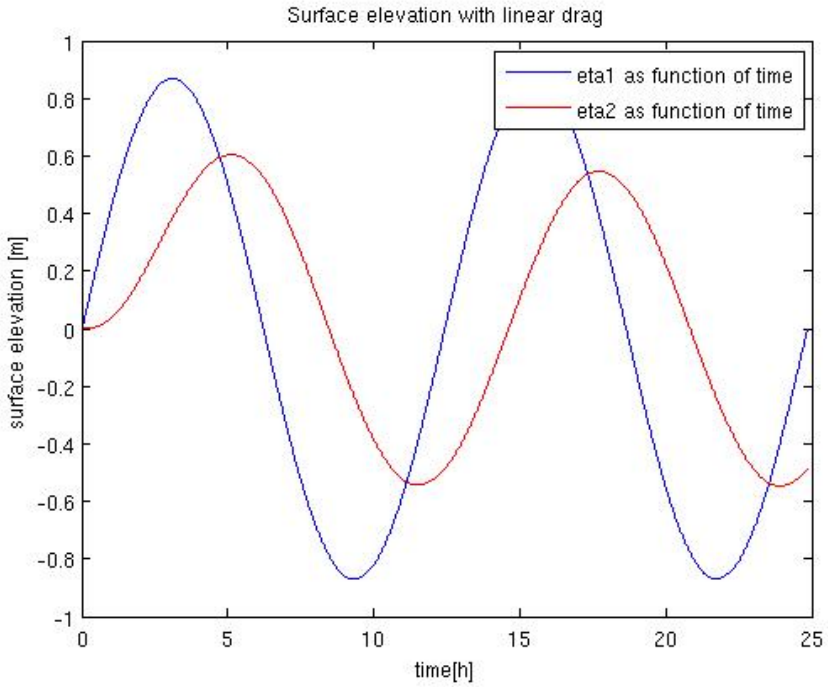

Figure 3.2: η_1 and η_2 plotted over two tidal cycles

The figure shows that the amplitude of the wave η_2 is smaller than the amplitude of η_1 and that there is a phase lag between the waves. The first maximum of η_2 is larger than the second one. This is because of the transient terms of Equation (3.7). After one tidal cycle the transient terms will be negligible and the other terms of the differential equation will dominate. It is then possible to find suitable expressions for the time delay and reduction factor compared to η_1. By using trigonometric relations on Equation (3.7), the time delay can be expressed by

$$T = \tan^{-1}\left(\frac{\frac{L_C D\omega_{M_2}}{g} + \frac{RCL_C}{g}}{\eta_{M_2} + \frac{RDL_C}{g} - \frac{L_C C\omega_{M_2}}{g}}\right)/\omega_{M_2} \ .$$

This gives $T \approx 131,5$ min which means that the η_2 wave is delayed with 131.5 min compared to the η_1 wave. The reduction factor can by the same trigonometric relations be expressed as

$$RF = \left(\sqrt{(-\frac{L_C C\omega_{M_2}}{g} + \frac{RDL_C}{g} + \eta_{M_2})^2 + (\frac{DL_C\omega_{M_2}}{g} + \frac{RL_C C}{g})^2)}\right)/\eta_{M_2}$$

which gives the value $RF = 0.629$ so we see from this that the amplitude is clearly decreased compared to the incoming wave η_1.

The velocity U_C in the channel is given in Figure 3.3:

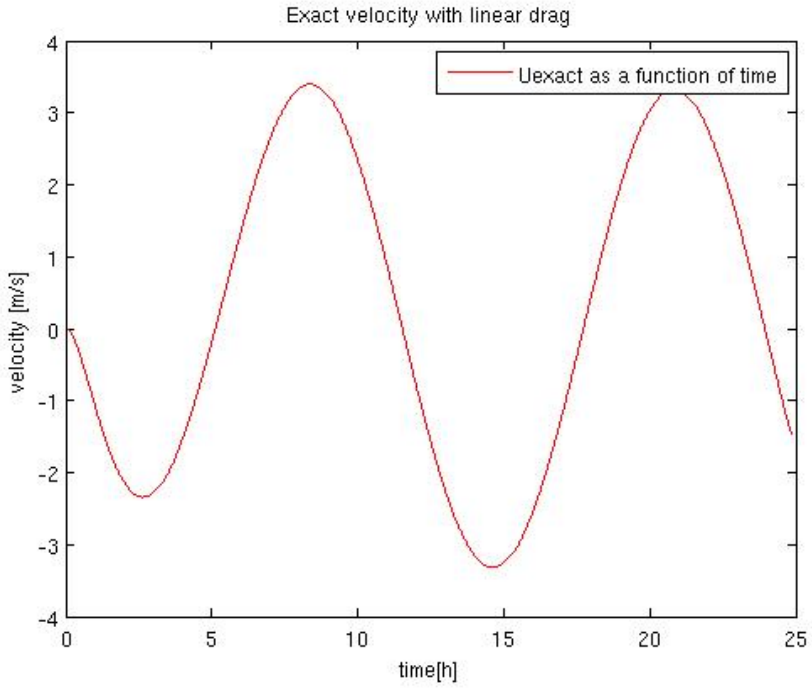

Figure 3.3: Velocity U_C plotted over two tidal cycles

We see that the plot suggests a maximum velocity through the channel close to 3.5 m/s. The maximum velocity occurs when the second derivative of η_2 is zero, that is, in the inflection point for η_2.

From Equation (3.4), the numerical solution of the same problem can be calculated. This has been done to investigate the error involved when computing approximations with the trapezoidal method, since this method also will be applied in the next section. From the discussion in the appendix we have that the trapezoidal method is a stable and neutral method. The error between the numerical and analytical solution was plotted for several time steps.

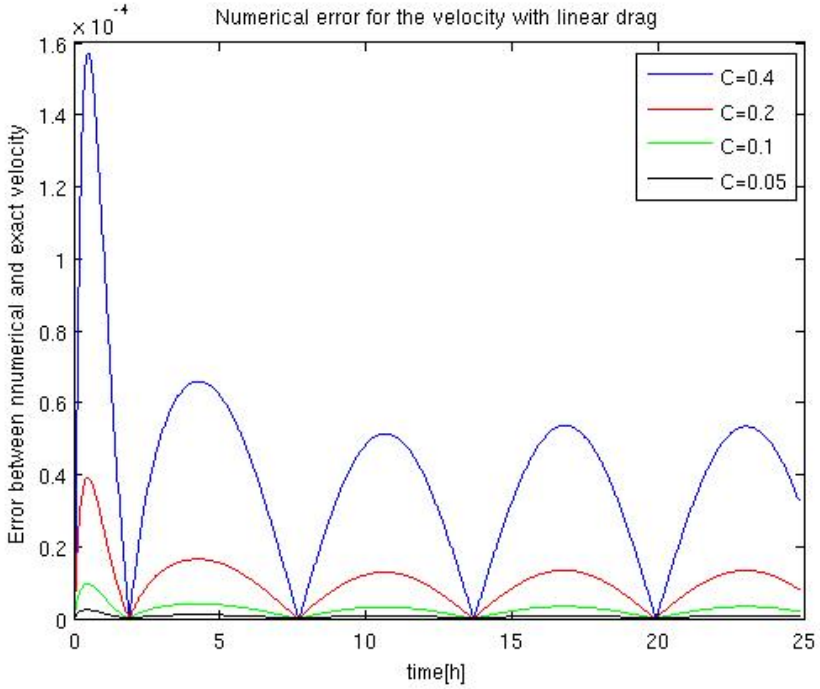

Figure 3.4: Error plotted for several Courant numbers

The Courant number is given by $C = \frac{\sqrt{gH}\Delta t}{L_C}$. The computation was performed with C=0.4, 0.2, 0.1 and 0.05, and the corresponding errors are given in Figure 3.4. The order of convergence P was found by taking the amplitude of each error plot and divide it by each other. The error E for a given difference scheme is given by $E = K\Delta t^P$ where K is a constant. Suppose E_0 is the error corresponding to $C = 0.4$ and E_1 the error corresponding to $C = 0.2$. P was estimated by taking

$$\frac{E_0}{E_1} = \frac{\Delta t^P}{(\frac{\Delta t}{2})^P} = 2^P \Rightarrow P = log_2\left(\frac{E_0}{E_1}\right) . \tag{3.8}$$

The same procedure was used for the other errors to give the following table:

C	E	P
$C = 0.4$	$1.5692 * 10^{-4}$	
$C = 0.2$	$3.9219 * 10^{-5}$	2.0004
$C = 0.1$	$9.8050 * 10^{-6}$	2.0000
$C = 0.05$	$2.4512 * 10^{-6}$	2.0000

Table 3.3: The order of convergence for the linear case

The order of convergence is approximately two, which is what we expect for the second order trapezoidal rule.

3.1.1 Neglect of the drag coefficient

If the drag coefficient R was equal to zero, the roots of the two equations in (3.2) would be imaginary and complex conjugate to each other. This would give the solutions

$$\begin{aligned} U_C &= \frac{b}{\omega_{M_2}^2 - a}\cos(\omega_{M_2} t) - \frac{b}{\omega_{M_2}^2 - a}\cos(\sqrt{a}t) \qquad \text{and} \\ \eta_2 &= \frac{L_C}{g}\left[\frac{\sqrt{a}b}{\omega_{M_2}^2 - a}\sin(\sqrt{a}t) - \frac{\omega_{M_2} b}{\omega_{M_2}^2 - a}\sin(\omega_{M_2} t)\right] + \eta_{M_2}\sin(\omega_{M_2} t)\ . \end{aligned} \tag{3.9}$$

The constants a and b are given as $a = \frac{g}{L_C}\frac{A_C}{A_2}$ and $b = \frac{g}{L_C}\eta_{M_2}\omega_{M_2}$. Thus we see that the velocity through the channel and the surface elevation in the basin always will be affected by another local mode as well as the incoming mode ω_{M_2}. This mode is the natural frequency of the system. Without the friction term this mode is not damped out and gives a contribution to the solution. The solutions for U_C and η_2 are given in Figure 3.5 and Figure 3.6 respectively.

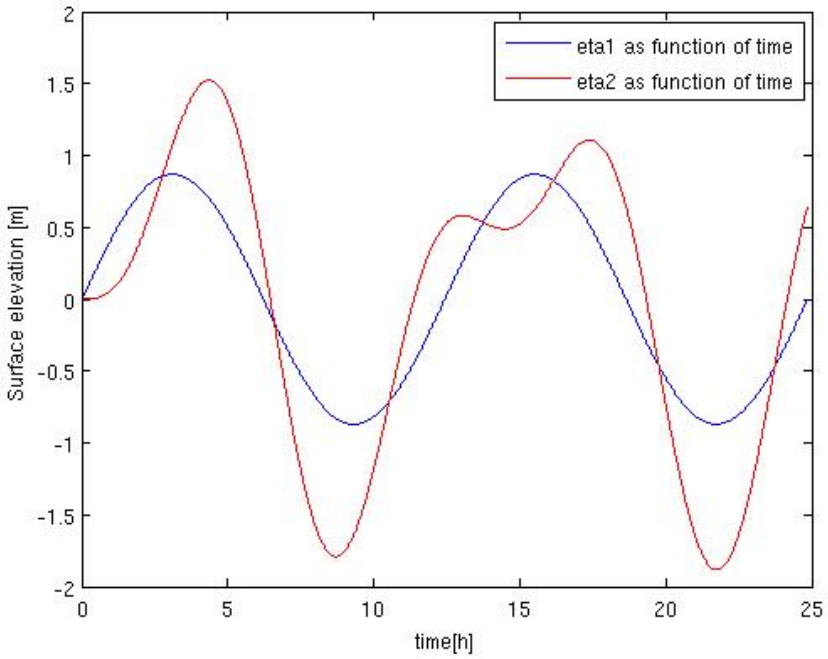

Figure 3.5: η_1 and η_2 plotted over two tidal cycles without drag

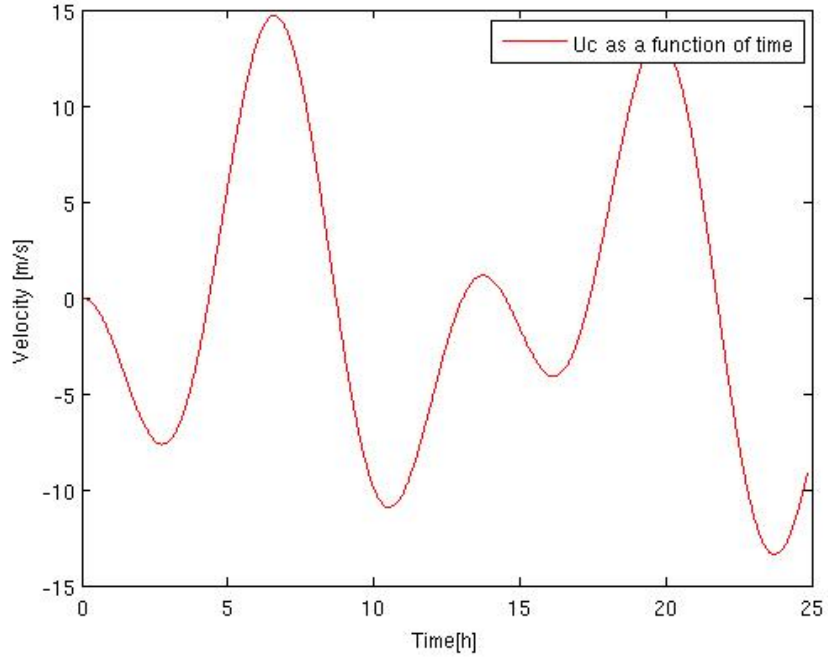

Figure 3.6: U_C plotted over two tidal cycles without drag

The figures show that the maximum and minimum are generally larger for the solutions without drag compared with the solutions for the linear drag, which is obvious. We notice the extra small jumps that occur after approximately 15 hours in the solution for both velocity and surface elevation. They occur due to the two different modes that drive the solution. When they have different sign we have negative interference between them and when they have the same sign we have positive interference between them. At the small peaks we have negative interference between the modes and they weaken each other.

For the two solutions, we notice that the denominator consists of the M_2-frequency and the local frequency. Suppose they were equal, we would get resonance between the two modes and the solution would go to infinity. This phenomenon will also be discussed in the section about seiches.

3.2 Inlets with quadratic drag coefficient

By assuming a quadratic friction term, we get the following equations:

$$\begin{aligned} \frac{d\eta_2}{dt} &= -\frac{A_C U_C}{A_2}\,, \\ \frac{dU_C}{dt} &= g\frac{\eta_2 - \eta_1}{L_C} - RU_C|U_C|\,. \end{aligned} \tag{3.10}$$

The constant R still represents the friction drag but now it has unit m^{-1}. The problem is nonlinear so we are not able to find an analytical solution. However, η_2 is not included in the nonlinear term so we can solve for this without problems. When doing a discretization with the trapezoidal rule, the problem has been split in a problem A and a problem B with a predictor-corrector method. The solution has been found in two steps by first finding a predictor value from problem A. The solution of this problem has been used as the initial guess when solving problem B. Problem B refined the predictor value by the corrector step.

$$\begin{aligned} \frac{\eta_2^{n+1} - \eta_2^n}{\Delta t} &= -\frac{A_C}{A_2}\frac{U_C^{n+1,P} + U_C^n}{2}\,, \\ \frac{U_C^{n+1,P} - U_C^n}{\Delta t} &= \frac{g}{2L_C}(\eta_2^{n+1} + \eta_2^n - (\eta_1^{n+1} + \eta_1^n))\,. \end{aligned} \tag{3.11}$$

The solution of η_2 and $U_C^{n+1,P}$ is found by the same method as for the linear case in section 3.1 so this is a second order method. To find the solution for U_C in step 2, $U_C^{n+1,P}$ is substituted

for the unknown value in the quadratic term.

$$\frac{U_C^{n+1} - U_C^{n+1,P}}{\Delta t} = -\frac{R}{2}(U_C^{n+1} + U_C^{n+1,P})|U_C^{n+1,P}| \, .$$

This gives the solution for U_C and η_2 but due to the implicitness of the method it is now a first order method. To symmetrize over a double time step, Strang-splitting is applied, see Istvan [15]. This means that in the next time step the two steps for solving the problem have been done in the opposite way. This means the value of U_C has been found by first finding a predictor from the equation with the nonlinear term.

$$\frac{U_C^{n+1,P} - U_C^{n}}{\Delta t} = -\frac{R}{2}(U_C^{n+1,P} + U_C^{n})|U_C^{n}| \, .$$

To find U_C and η_2, Equation (3.11) has been used, except that $U_C^{n+1,P}$ is substituted with U_C^{n+1} and U_C^n is substituted with $U_C^{n+1,P}$. The Strang splitting has been applied to make the results as accurate as possible.

We still consider Saltstraumen so the values for the constants in Table 3.2 in the previous section are also used here. When the surface elevation was plotted against time we got the following:

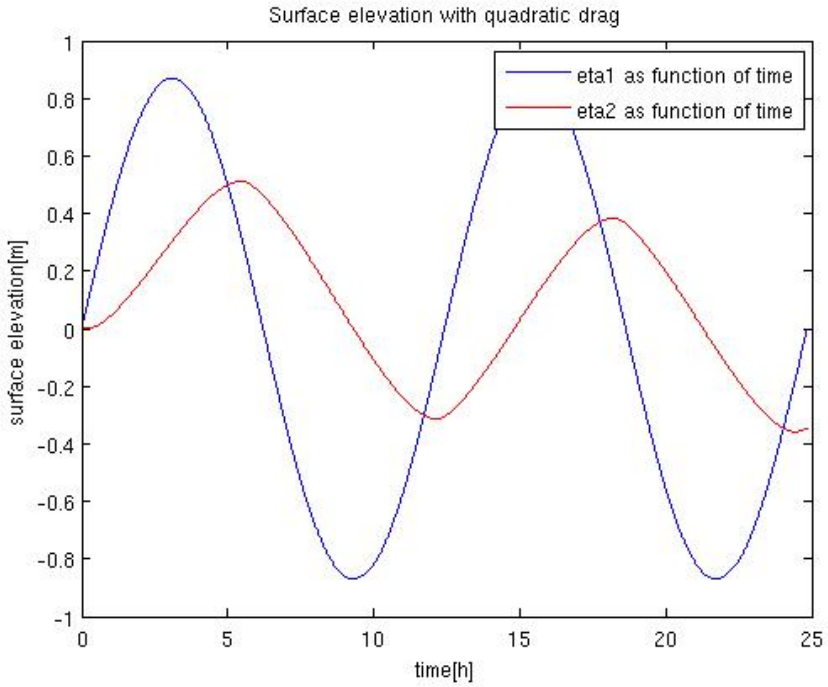

Figure 3.7: η_1 and η_2 plotted over two tidal cycles with quadratic drag

The amplitude of η_2 is smaller compared to the linear case. The plot gives that η_2 has a maximum value around 0.38 m. Here we have ignored the first peak because of the contribution from the transient terms. The reduction factor of η_2 is therefore about $RF = \frac{0.38}{\eta_{M_2}} \approx 0.44$ so we see that the reduction factor is smaller than in the linear case. The phase delay for the quadratic drag was calculated in matlab by checking for which index the surface elevation was zero for η_1 and η_2. Then the indexes were converted to time and the difference between the two waves was calculated. This gave a phase delay of $2.63 * 60\text{min} \approx 158$ min which is a longer phase delay than for the linear case.

The velocity through Saltstraumen is given in Figure 3.8

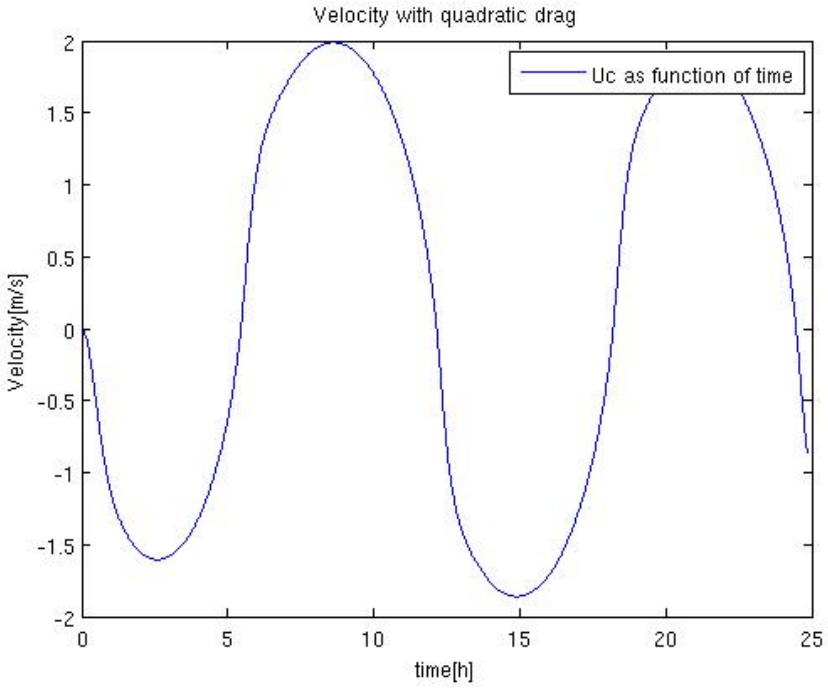

Figure 3.8: Velocity U_C plotted over two tidal cycles

When the friction is quadratic, we get a maximum velocity of about 2 ms^{-1} through the channel when the second derivative of η_2 is zero, that is, in the inflection point of η_2. This is less than what we had for the linear case, as we also expect.

The trapezoidal method is stable and neutral. From the previous section, we found that the method converged to the analytical solution as we chose the time step smaller. In this case, we cannot compare the numerical solution with an analytical one since the problem

makes it impossible to compute an analytical solution. However, we know that the method still is neutral and stable. To investigate if the method still converges to the correct solution, the solutions for different time steps can be plotted and the error between them can be found. The order of convergence can be found in the same way as in the previous section. If the error between two time steps decreases as the time step gets smaller, it can be concluded that the method converges for the nonlinear problem as well as the linear problem. The error is plotted in Figure 3.9.

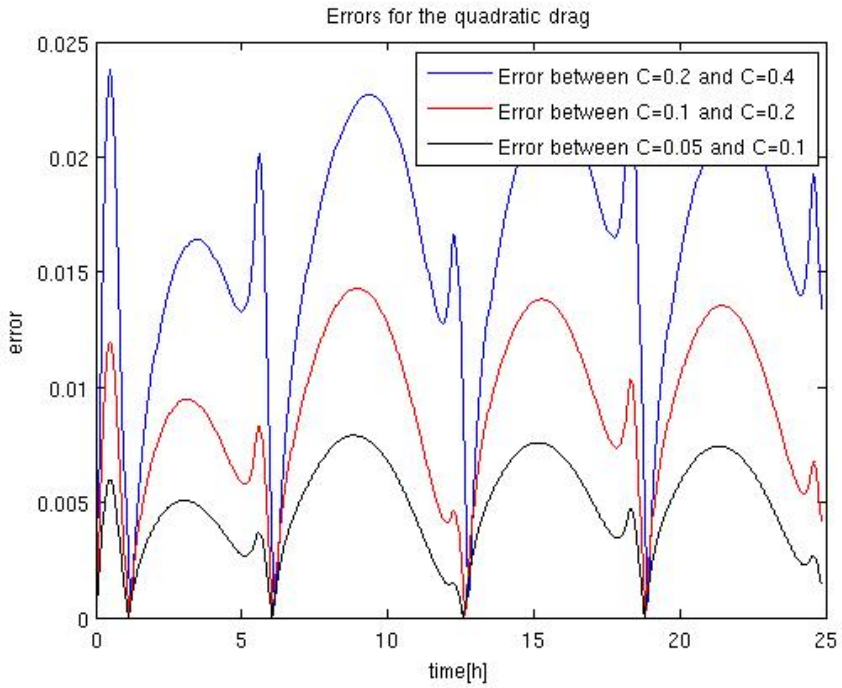

Figure 3.9: Error for U_C for several Courant numbers

The error clearly decreases as the Courant-number gets smaller. On the error plot, small jumps repeatedly occurs. These are due to phase errors. As the time steps are different for the 4 solutions, their phase also get slightly different. The jumps on the plot coincide with the inflection points for the velocity in Figure 3.8. That is, where the increase or decrease of the velocity is largest. The difference between the velocities is large at these points, and so the phase errors also get most apparent at these points.

The order of convergence was found by comparing the errors for the different Courant-numbers with each other. The theory for the order of convergence is the same as for the linear case, that is, the order of convergence P has been found by taking $P = \log_2 \frac{E_0}{E_1}$. In the quadratic

case, E_0 is the error between the numerical solution for C=0.05 and C=0.1 and E_1 is the error between the numerical solution for C=0.1 and C=0.2. The errors were found in a different way than for the linear case. Instead of comparing the amplitudes of the errors, the errors from each time step were compared to find a P-value for each time step. Then the average was calculated to find the P-value for the method. Since the error is calculated based on two numerical solutions and not compared with an analytical solution, the order of convergence only gives an indication of how accurate the method is in the quadratic case. The following table shows the order of convergence for the solution for the velocity. It is expected that the solution for η_2 will give results of the same magnitude.

	P
Error between C=0.4 and C=0.2	
	0.8630
Error between C=0.2 and C=0.1	
	0.9568
Error between C=0.1 and C=0.05	

Table 3.4: The order of convergence for the quadratic case

The order of convergence is close to one which is what we expected.

3.3 Seiches

A seiche is a standing wave that can be formed by the superposition of two waves with the same wavelength which propagate in opposite directions. This can occur in a basin like Skjerstadfjorden. If the frequency of this wave is the same as the frequency of the incoming Kelvin wave, the two waves can get into resonance. This scenario will be discussed here. An appropriate sketch of the problem is illustrated in Figure 3.10.

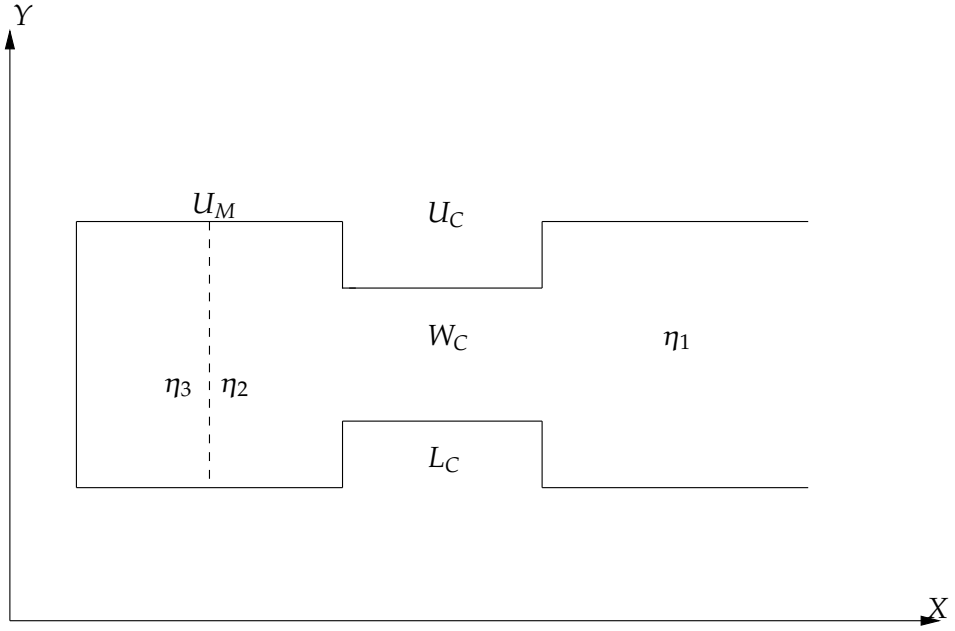

Figure 3.10: Example of a Box model situation with seiches

U_M is the velocity of the current in the fjord and η_3 is the surface elevation innermost in the fjord. When describing this problem, we need two more equations. The friction drag will be neglected. This gives the following set:

$$\begin{aligned}
\frac{d\eta_2}{dt} &= -\frac{A_C U_C}{A_2} + \frac{A_F U_M}{A_2}\,, \\
\frac{dU_C}{dt} &= g\frac{\eta_2 - \eta_1}{L_C}\,, \\
\frac{dU_M}{dt} &= g\frac{\eta_3 - \eta_2}{L_F}\,, \\
\frac{d\eta_3}{dt} &= -\frac{A_F U_M}{A_2}\,.
\end{aligned} \tag{3.12}$$

A_F is the cross-sectional area of the fjord while L_F is the length of the fjord. The initial conditions are the same as before, that is, U_C, U_M, η_2 and η_3 are zero when t=0. By solving for η_2, we get the following differential equation

$$\eta_2'''' + K\eta_2'' + E\eta_2 = Q\sin(\omega_{M_2} t)$$

where the constants K,E and Q are given in Table 3.5. We see that when this equation is solved we get four imaginary roots where two and two are complex conjugate of each other.

The solution is

$$\eta_2 = C_1\cos(r_1 t) + C_2\sin(r_1 t) + C_3\cos(r_2 t) + C_4\sin(r_2 t) + \frac{Q\sin(\omega_{M_2} t)}{-K\omega_{M_2}^2 + E + \omega_{M_2}^4}\ . \quad (3.13)$$

where r_1 and r_2 are the roots of the characteristic polynomial of the differential equation. The particular solution is carried out by the use of www.wolframalpha.com. From η_2, the solutions for η_3, U_C and U_M can be found by using the relations

$$\begin{aligned} U_C =& \frac{g}{L_C}[\frac{C_1}{r_1}\sin(r_1 t) - \frac{C_2}{r_1}\cos(r_1 t) + \frac{C_3}{r_2}\sin(r_2 t) - \frac{C_4}{r_2}\cos(r_2 t) \\ & - \frac{Q}{\omega_{M_2}}\frac{\cos(\omega_{M_2} t)}{-K\omega_{M_2}^2 + E + \omega_{M_2}^4} + \frac{\eta_{M_2}}{\omega_{M_2}}\cos(\omega_{M_2} t)]\ , \\ U_M =& \frac{A_2}{A_F}\frac{d\eta_2}{dt} + \frac{A_C}{A_F}U_C\ , \\ \eta_3 =& \frac{L_F}{g}\frac{dU_M}{dt} + \eta_2\ . \end{aligned}$$

The constants used for this problem are given in Table 3.5.

$$\begin{aligned} L_F &= \sqrt{A_2} \\ A_F &= 400 L_F \\ K &= AC + 2BD \\ E &= BDAC \\ Q &= BDAC\eta_{M_2} - AC\eta_{M_2}\omega_{M_2}^2 \\ A &= \tfrac{A_C}{A_2} \\ B &= \tfrac{A_F}{A_2} \\ C &= \tfrac{g}{L_C} \\ D &= \tfrac{g}{L_F} \\ C_1 &= 0 \\ C_3 &= C_1 \\ C_4 &= \frac{\frac{r_1^2 C}{\omega_{M_2}}\frac{1}{-K\omega_{M_2}^2+E+\omega_{M_2}^4} - \frac{r_1^2\eta_{M_2}}{\omega_{M_2}} - \frac{Q\omega_{M_2}^2}{-K\omega_{M_2}^2+E+\omega_{M_2}^4}}{r_2 - \frac{r_1^2}{r_2}} \\ C_2 &= \tfrac{1}{r_1}(\frac{-Q\omega_{M_2}^2}{-K\omega_{M_2}^2+E+\omega_{M_2}^4} - r_2 C_4) \end{aligned}$$

Table 3.5: Constants used for the problem with seiches

The two constants L_F and A_F are the two new constants that have to be given a value. L_F was set by assuming that Skjerstadfjorden was quadratic while A_F was set by assuming that the depth in Skjerstadfjorden was about 400 meters deep. The constants C_1, C_2, C_3, and C_4

are found from the initial conditions. The solutions for the 4 variables were plotted over 10 tidal cycles.

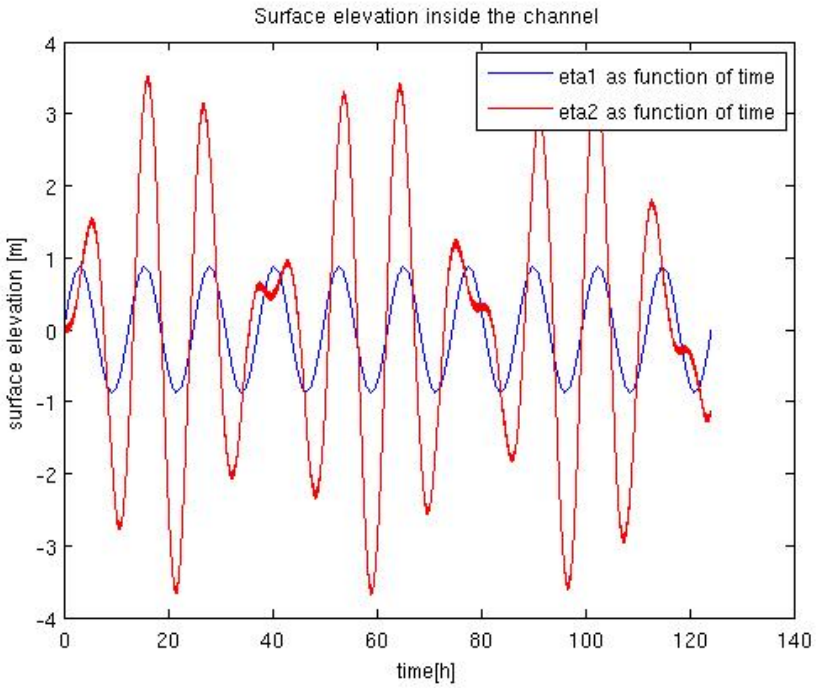

Figure 3.11: Surface elevation η_2 plotted over 10 tidal cycles

The roots of η_2 are $r_1 \approx 6,03 * 10^{-3}\text{s}^{-1}$, $r_2 \approx 1,84 * 10^{-4}\text{s}^{-1}$ and $\omega_{M_2} \approx 1,4 * 10^{-4}\text{s}^{-1}$. The roots r_1 and r_2 are naturally occurring frequencies of the system. They can for instance occur due to local seiches in the fjord. We see that r_2 and ω_{M_2} are the two "low" frequencies while r_1 is the "high" frequency. We also notice that the amplitudes corresponding to the sine-terms with the r_2 and ω_{M_2} modes are much larger than the amplitude corresponding to the sine-term with the r_1 mode. For the first two periods, it seems to be a large difference on the surface elevation, while for the third and fourth period the difference is much smaller. This behavior continues as the time goes. The explanation for this behavior is due to the "low" frequencies. The two frequencies can either cause positive or negative interference. When they give the same sign on the sine-terms we have positive interference. This will give large surface elevations of η_2. However, when the sine-terms have opposite signs we have negative interference and the surface elevation will be smaller. For the negative interference, the behavior of the r_1-mode will be more apparent. This creates the small oscillations that looks like noise in Figure 3.11. Compared to the previous solutions with linear and quadratic drag, the amplitude of η_2 has increased. When neglecting the drag, more modes than only

the M_2-mode are affecting the solution. When the frequencies corresponding to these modes give positive interference with the M_2-mode, the amplitudes increase. This effect will also be shown on the next plot:

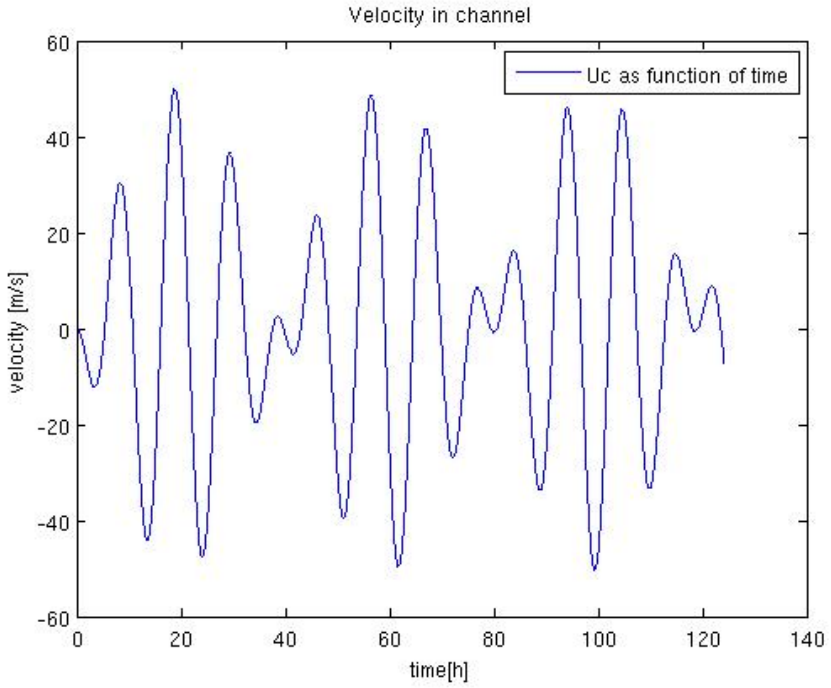

Figure 3.12: Velocity U_C plotted over 10 tidal cycles

The velocity is very large at its maximum. The explanation follows again from the "low frequencies". Theoretically, in an undamped system, full resonance, that is if the frequencies were equal, would allow unlimited adding of energy to the system. Therefore, if two of the modes had become equal the velocity would go to infinity.

The solutions for η_2 and η_3 are expected to be very similar because they both describe how the current propagates in the fjord. The difference between the surface elevations is given in the next plot:

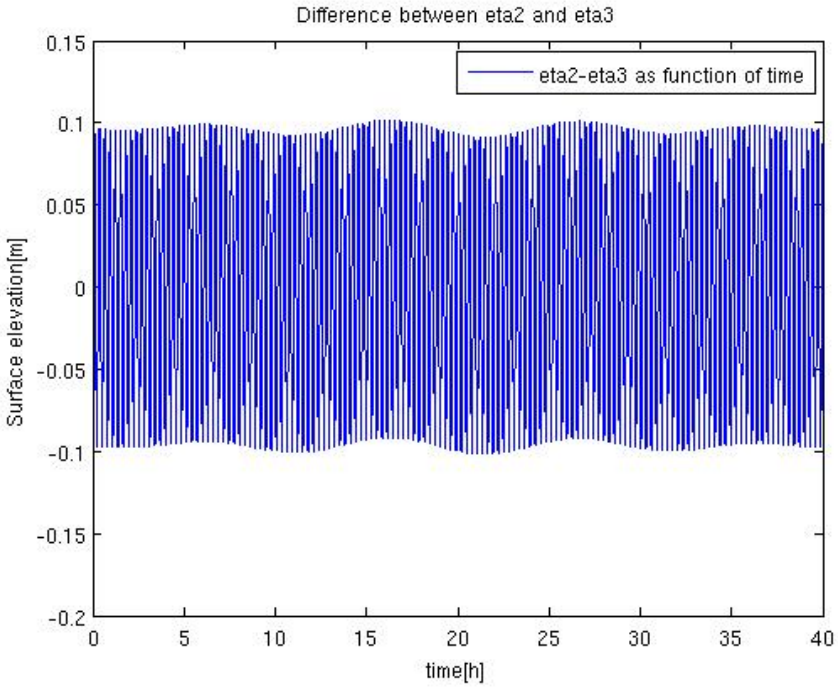

Figure 3.13: The difference between η_2 and η_3 over 40 hours

The plot is only taken for the first 40 hours to show the behavior we want to describe. As expected, the difference between the two waves is very small. The oscillations on the plot are due to the high frequent r_1-mode in the solution. This will be explained after the next plot. The velocity in the fjord U_M is depending on the height difference between η_2 and η_3. We therefore also expect this velocity to be small. The solution is given in Figure 3.14:

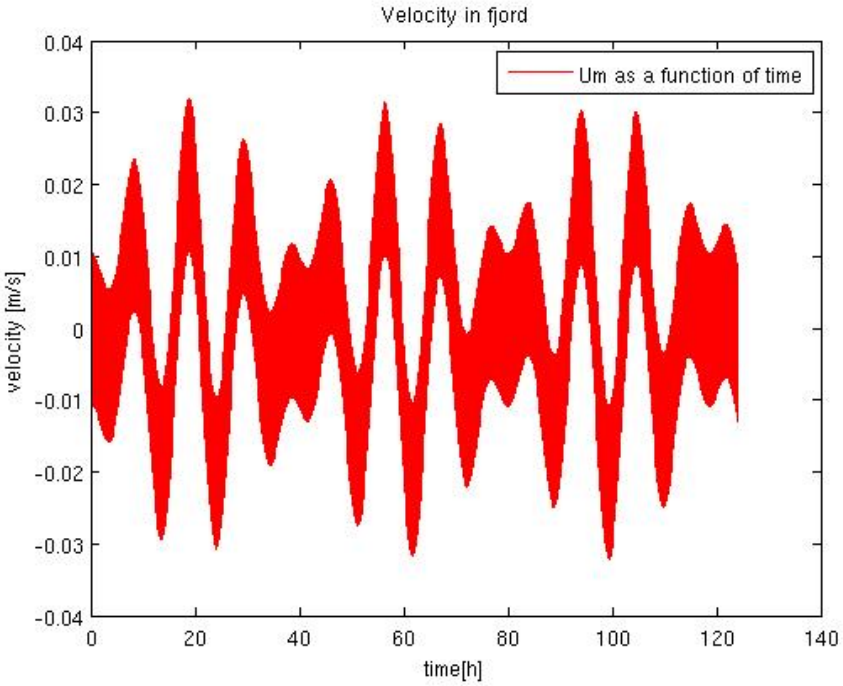

Figure 3.14: Velocity U_M plotted over 10 tidal cycles

The velocity in the fjord is very low. We also notice that the oscillations of the solution is clearly appearing. In the fjord, the amplitude corresponding to the r_1-mode with high frequency is of the same magnitude as the two other modes. This mode does therefore have much more impact on the solution in this case. Since this mode has much shorter period than the other modes, the oscillations on Figure 3.14 are created.

By tuning the constants used for the problem, resonance can be achieved between the ω_{M_2}-mode and the r_2-mode. By tuning the value of W_C, the width of the channel to 192 m, the system was manipulated to get $r_2 = 1.401 \cdot 10^{-4}$ s$^{-1} \approx \omega_{M_2}$. This is equivalent to resonance between those two modes. The result gave the following plot for U_C.

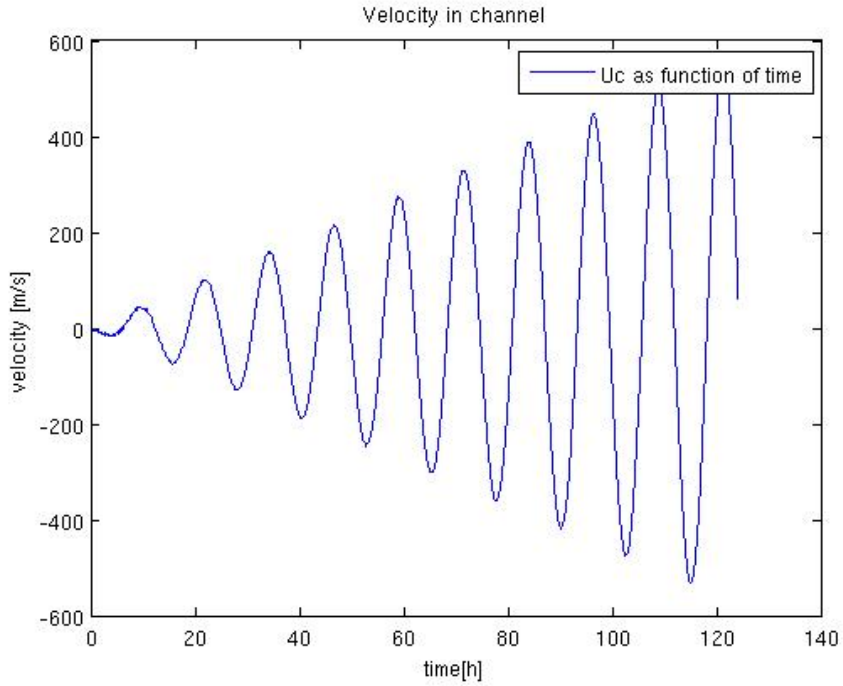

Figure 3.15: Velocity U_C plotted over 10 tidal cycles with resonance

The velocity tends to increase towards infinity as time goes. This scenario is of course impossible in real life. In real life the friction drag would be included and as we have seen earlier the driving modes would only be the M_2-mode since the local modes r_1 and r_2 would die out due to the friction.

Chapter 4

The modified Bergen Ocean Model(BOM)

For the rest of this thesis, we will consider a modified version of the Bergen Ocean Model(BOM), see Berntsen [4], to investigate the inlets in the area around Bodø and Lofoten. This will be applied to find the kinetic and potential energy fluxes in the Lofoten area. Potential and kinetic energy through transects will be considered. The distribution of kinetic and potential energy flux over the total area will also be discussed. At last the energy dissipation due to bottom friction and viscosity will be considered. In the next chapter, the tide in Saltstraumen will be discussed with the results from Chapter 3 kept in mind.

4.1 The model and its boundary conditions

The model is a two-dimensional depth integrated version of the BOM that solves the shallow water equations on transport form. This means that the equations for the x- and y-directions are also integrated in the z-direction and solved for the transports $\int_0^h u dz$ and $\int_0^h v dz$ instead of $[u, v]$. We already know from Chapter 2 that u and v are independent of z so the integrals become uh and vh respectively. On transport form, the equations developed in Chapter 2 take the form

$$\frac{\partial \eta}{\partial t} + \frac{\partial}{\partial x}(hu) + \frac{\partial}{\partial y}(hv) = 0 \,, \tag{4.1}$$

$$\frac{\partial (uh)}{\partial t} + \mathbf{U_H} \cdot \nabla (uh) - fvh = -gh\frac{\partial \eta}{\partial x} + \frac{\partial}{\partial x}(A_{M2D}\frac{\partial (uh)}{\partial x}) + \frac{\partial}{\partial y}(A_{M2D}\frac{\partial (uh)}{\partial y}) \,, \tag{4.2}$$

$$\frac{\partial (vh)}{\partial t} + \mathbf{U_H} \cdot \nabla (vh) + fuh = -gh\frac{\partial \eta}{\partial y} + \frac{\partial}{\partial x}(A_{M2D}\frac{\partial (vh)}{\partial x}) + \frac{\partial}{\partial y}(A_{M2D}\frac{\partial (vh)}{\partial y}) \,. \tag{4.3}$$

The equations are still mathematical equivalent to the equations developed in Chapter 2. Some new terms have been introduced:

$$F_x = \frac{\partial}{\partial x}(A_{M2D}\frac{\partial(uh)}{\partial x}) + \frac{\partial}{\partial y}(A_{M2D}\frac{\partial(uh)}{\partial y}) \tag{4.4}$$

and

$$F_y = \frac{\partial}{\partial x}(A_{M2D}\frac{\partial(vh)}{\partial x}) + \frac{\partial}{\partial y}(A_{M2D}\frac{\partial(vh)}{\partial y}) \ . \tag{4.5}$$

These terms are the viscosity terms. When modeling a problem like this, much of the energy dissipation occurs by motion at subgrid scales. In [6] it is stated that to count for energy losses from both the Reynolds stress and the motion at subgrid scales, a much larger viscosity called the eddy viscosity is introduced. The horizontal viscosities cover a much larger distance of unresolved motion than the vertical viscosities and the vertical viscosity is therefore neglected. A_{M2D} is referred to as the two-dimensional eddy viscosity. This viscosity can either be set as a constant or it can be expressed according to Smagorinsky, see [19]:

$$A_{M2D} = C_M \Delta x \Delta y \frac{1}{2}\left[\left(\frac{\partial u}{\partial x}\right)^2 + \frac{1}{2}\left(\frac{\partial v}{\partial x} + \frac{\partial u}{\partial y}\right)^2 + \left(\frac{\partial v}{\partial y}\right)^2\right]^{\frac{1}{2}} \ , \tag{4.6}$$

where C_M is the Smagorinsky constant and Δx and Δy are grid spaces.

The model applies a two-dimensional grid with 1800 grid points in the x-direction and 1300 grid points in the y-direction. The grids are evenly spaced with dx=dy=250 m. The dominating mode for the system is the M_2-mode. The remaining tidal modes are neglected. The Coriolis parameter f is set to be $f = 1.3 * 10^{-4}$ s^{-1}. The model uses different subroutines to solve the linear terms and the nonlinear terms separately. To solve the linear terms of the equations, a predictor-corrector method is applied for the time steps. In the first time step, the forward Euler is used as a predictor and in the later time steps the leapfrog scheme is used as a predictor. The trapezoidal method is used as a corrector for all time steps. The nonlinear terms have been computed with a total variation diminishing(TVD) scheme to avoid overshoot and undershoot. Overshoot and undershoot are uncontrolled growth of the solution that causes instability. Suppose we have a solution q that propagates over time. As suggested in Barthel [3], the total variation of a scheme is a measure of the amount of oscillations in the field q.

$$TV(q^n) = \sum_{j=2}^{J} |q_j^n - q_{j-1}^n| \ .$$

If $TV(q^{n+1}) \leq TV(q^n)$ we have a TVD scheme. Suppose there is a shock in the solution q. The schemes handle this shock differently when trying to approximate the solution. This can then cause an overshoot for some schemes. Therefore flux limiters $\phi(\theta)$ are introduced where

θ is a so-called smoothness indicator to smooth the shock. To make sure the method is TVD, the model applies the superbee flux limiter, see Barthel [3] and Sweby [20],

$\phi(\theta) = max[0, min(1, 2\theta), min(2, \theta)]$.

It uses the largest possible steepening, without getting overshoot or undershoot, to represent the shock. The nonlinear terms in Equation (4.2) and Equation (4.3) are

$$\mathbf{U_H} \cdot \nabla(uh) = u\frac{\partial(uh)}{\partial x} + v\frac{\partial(uh)}{\partial y}$$

and

$$\mathbf{U_H} \cdot \nabla(vh) = u\frac{\partial(vh)}{\partial x} + v\frac{\partial(vh)}{\partial y} \ .$$

The model expresses these terms on conservative form.

$$\frac{\partial(uuh)}{\partial x} + \frac{\partial(uvh)}{\partial y}$$

and

$$\frac{\partial(uvh)}{\partial x} + \frac{\partial(vvh)}{\partial y} \ .$$

Generally for a 3-dimensional flow we have by the product rule

$$\begin{aligned} &\frac{\partial(uuh)}{\partial x} + \frac{\partial(uvh)}{\partial y} + \frac{\partial(uwh)}{\partial z} \\ &= u\frac{\partial(uh)}{\partial x} + v\frac{\partial(uh)}{\partial y} + w\frac{\partial(uh)}{\partial z} + (uh)\nabla \cdot \mathbf{U} \ . \end{aligned} \tag{4.7}$$

From Chapter 2 we have that $\nabla \cdot \mathbf{U} = 0$ which gives that the equality holds in a 3-dimensional flow. We also have that the horizontal velocity field is z-independent. By assuming that the term $uh\frac{\partial w}{\partial z}$, which occurs from the term $\frac{\partial(uwh)}{\partial z}$, is small the equality also holds for a 2-dimensional flow. This gives that the two expressions for the nonlinear terms are mathematical equivalent. By having the equations on this form makes the model more robust. When having the equations on this form they have been solved by the upwind scheme and the Lax-Wendroff scheme in space before the solution is propagated over time with the TVD-scheme. The upwind scheme is first order accurate and the Lax-Wendroff scheme is second order accurate. However, the upwind scheme is monotonic. A monotonic scheme is a scheme where the maximum values and the minimum values do not change throughout an iteration. It follows that the upwind scheme has no problems with overshoot and undershoot. The Lax-Wendroff scheme do have problems with this. Therefore the TVD-scheme uses flux limiters that decide the weights(which scheme that should be used the most) of the two numerical schemes. The Lax-Wendroff scheme is best when the solution is smooth, but when there

are shocks in the solution, the upwind scheme is weighted more to avoid the overshoot and undershoot.

A staggered grid has been used to do the calculations in the spatial steps for both the linear and the nonlinear terms, that is the values of u, v and η are placed in different spots of the grid. This means, solving for instance for η, the values of u and v need to be interpolated to the η-value and vice versa when we are solving for u and v. This model uses the Arakawa C-grid for this interpolation, see [4, 6].

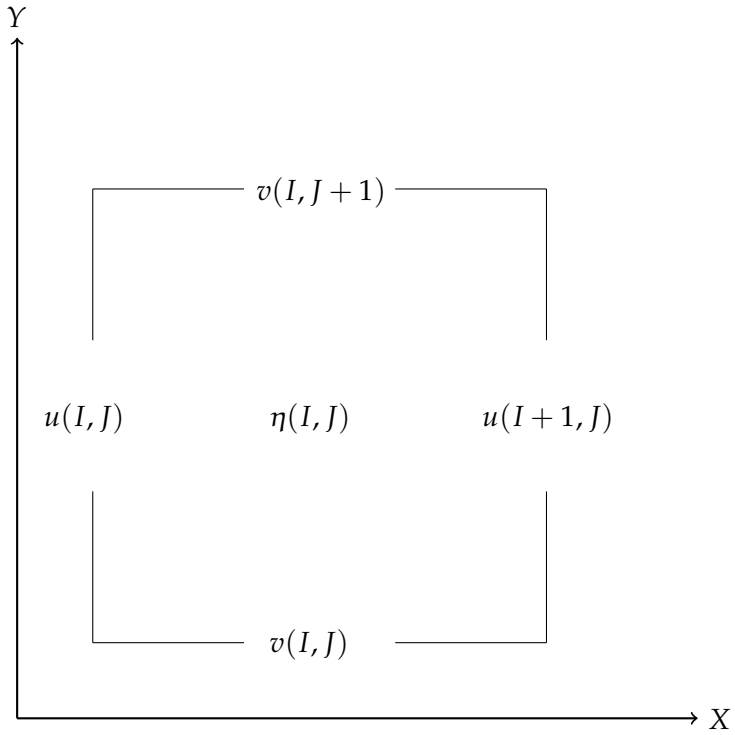

Figure 4.1: The location of the variables in the staggered grid

The variables h and A_{M2D} are defined in η-points. The C-grid is very beneficial when dealing with flows. Since the velocities u and v are placed at the end of the cells we know that the flux that goes out of one cell is the same as the flux that comes into the next cell.

4.1.1 Boundary conditions

In Chapter 2 we stated the condition for the vertical velocity w to be zero at the bottom because of the impermeability. However, for the model there need to be stated some boundary conditions for the horizontal velocities at the bottom as well. At the bottom there will be a stress that affects the flow. In [6] and [4] it is suggested that the bottom stress $\boldsymbol{\tau_b}$ can be

written as

$$\boldsymbol{\tau_b} = \rho_0 C_D |\mathbf{U_b}| \mathbf{U_b} \ , \tag{4.8}$$

where $\mathbf{U_b}$ is the horizontal velocity at the bottom and C_D is the drag coefficient. The drag coefficient is set to be $C_D = 0.0025$.

For the numerical model, the calculations are quite straightforward as long as they are not on the boundary. However, on the open boundary, that is, in the open ocean there need to be stated some conditions. In Martinsen et al. [17] and Ali et al. [2], it is suggested that in the flow relaxation zones, that is in the boundary zone, the surface elevation can be updated at each time step according to

$$\Phi = (1 - \alpha)\Phi_{int} + \alpha\Phi_{ext} \ , \tag{4.9}$$

where Φ_{int} contains the unrelaxed values calculated by the model, while Φ_{ext} is the specified external value. The value of α is 1 at the open boundary and changes smoothly towards 0 at the inner end of the boundary zone. This method is called the flow relaxation scheme(FRS). The boundary zone is set to be 40 grid cells thick in the model. This means that at the inner end of cell 40 from the boundary, α is equal to zero and the calculations do only depend on the model.

4.2 The Lofoten area

The area being modeled reaches from just south of Bodø to just north of Lofoten. Bottom topography data from the Norwegian Hydrographic Service were used to generate the bottom matrix of the area. This matrix was loaded to matlab. First, the land was masked out by saying that everywhere the depth was larger than zero, the depth was set to 1. Everywhere on land, "depth" was set to -1. Then the contour function in matlab was used to plot the zero-contour of the bottom matrix. This gave the land boundary. Later, the contour-routine was used to plot contours at certain depths. The result is given in the following plot:

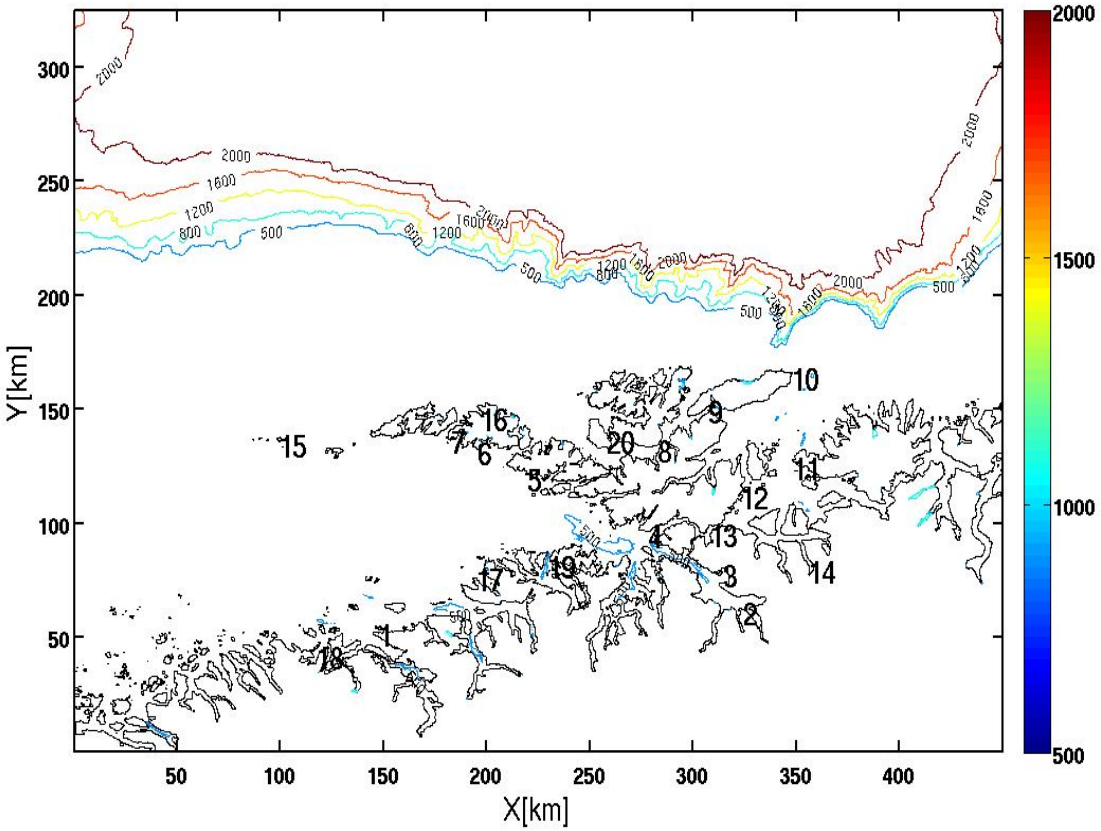

Figure 4.2: Contour-plot of the bottom matrix

The fjord on the inside of the Lofoten islands is called Vestfjorden. This is referred to repeatedly during the thesis. The colorbar on the right side of the plot shows how the color of the contours changes with depth in meters, that is, a dark red contour is plotted where the depth is about 2000 m. The figure shows that the continental shelf outside Lofoten is very steep. The numbers on the figure represent stations where measurements of the amplitude (that has been decomposed down to the M_2 frequency by Fourier transformation) of the surface elevation have been done. These elevations are also given in Moe et al [18]. The depth is also given. These data and the names of the stations corresponding to the numbers are given in the next table:

Number	Place	M_2-amplitude[m]	Depth[m]
1	Bodø	0.869	42.2
2	Narvik	0.993	32.59
3	Bogen	0.943	57.7
4	Lødingen	0.933	47.78
5	Kabelvåg	0.926	31.0
6	Stamsund	0.887	27.1
7	Ballstad	0.847	53.5
8	Sortland	0.663	34.4
9	Risøyhamn	0.677	32.26
10	Andenes	0.648	184.7
11	Skrolsvik	0.685	190.9
12	Harstad	0.693	44.72
13	Evenskjær	0.740	73.0
14	Røkenes	0.699	131.0
15	Røst	0.775	116.4
16	Tangstad	0.623	121
17	Helnessund	0.901	61
18	Inndyr	0.859	230.9
19	Skutvik	0.987	122.6
20	Stokmarknes	0.658	143

Table 4.1: List over M_2-amplitude and depth for the stations

The model was run several times, with the M_2-mode as the driving force, changing parameters until the amplitudes coincided with the measured amplitudes in Table 4.1. With these amplitudes, the model was run for 5 different values of A_{M2D}:100,10,1,0.1,0.01 $\mathrm{m^2 s^{-1}}$ to investigate how the amplitudes changed at places 1-20 in Figure 4.2. The result is given in the following table:

	Amplitudes[m]							
	Observed	Model						
A_{M2D}		$0.01\text{m}^2\text{s}^{-1}$			$0.1\text{m}^2\text{s}^{-1}$	$1\text{m}^2\text{s}^{-1}$	$10\text{m}^2\text{s}^{-1}$	$100\text{m}^2\text{s}^{-1}$
Bodø	0.869	0.885	0.867	0.877	0.877	0.878	0.878	0.881
Narvik	0.993	1.024	0.955	1.007	1.009	1.008	1.007	1.010
Bogen	0.943	1.017	0.950	1.002	1.004	1.003	1.003	1.006
Lødingen	0.933	0.988	0.916	0.974	0.975	0.974	0.974	0.979
Kabelvåg	0.926	0.942	0.902	0.928	0.929	0.929	0.930	0.933
Stamsund	0.887	0.925	0.887	0.908	0.908	0.909	0.910	0.914
Ballstad	0.847	0.914	0.882	0.900	0.901	0.901	0.902	0.906
Sortland	0.663	0.659	0.649	0.650	0.651	0.650	0.647	0.656
Risøyhamn	0.677	0.644	0.653	0.640	0.641	0.640	0.639	0.640
Andenes	0.648	0.619	0.627	0.620	0.620	0.620	0.620	0.622
Skrolsvik	0.685	0.642	0.671	0.643	0.643	0.643	0.643	0.644
Harstad	0.693	0.652	0.691	0.652	0.652	0.652	0.652	0.653
Evenskjær	0.740	0.664	0.750	0.701	0.701	0.700	0.702	0.723
Røkenes	0.699	0.664	0.720	0.667	0.667	0.667	0.663	0.666
Røst	0.775	0.747	0.740	0.747	0.744	0.744	0.747	0.757
Tangstad	0.623	0.638	0.643	0.642	0.642	0.642	0.641	0.641
Helnessund	0.901	0.915	0.892	0.907	0.907	0.907	0.907	0.909
Inndyr	0.859	0.875	0.858	0.866	0.866	0.867	0.867	0.871
Skutvik	0.987	0.955	0.917	0.944	0.945	0.945	0.945	0.949
Stokmarknes	0.658	0.647	0.644	0.645	0.645	0.644	0.643	0.646

Table 4.2: Amplitudes in meters

The table shows that the amplitudes are almost not affected by the different choices of A_{M2D}. For such a small eddy viscosity as $A_{M2D} = 0.01\text{m}^2\text{s}^{-1}$, the solution is stable. This is because of the bottom friction and the fact that the upwind scheme gives the model a numerical viscosity that damps the solution. The changes of amplitude are more apparent for the three first columns. These are all results from the calculations with $A_{M2D} = 0.01\ \text{m}^2\text{s}^{-1}$. They are ordered in the following way:

- Column 1 represents the solution when channels 2-6 in Table 4.4 are closed.
- Column 2 represents the solution when channel 2-Tjeldsundet has been made larger.
- Column 3 represents the usual solution with $A_{M2D} = 0.01\ \text{m}^2\text{s}^{-1}$.

For the first two points, the bottom matrix has been manipulated. First by claiming that the channels 2-6 have zero depth and second by saying that Tjeldsundet is a straight channel with depth of 200 meters and width of 2750 meters. One would probably expect that the first scenario would increase the amplitudes of the tide in Vestfjorden when the water is not allowed to go through the channels. Table 4.2 however, shows that the amplitudes are almost not affected by this. For instance in Narvik, which is in the inner end of Vestfjorden, the amplitude has only increased by approximately 1 cm compared to the other results from the model. For the second scenario, the amplitudes on the places located in Vestfjorden seem to decrease by 3-5 cm while the other amplitudes do not change significantly. The distribution of the mean surface elevation for the Lofoten area is given in the next figure.

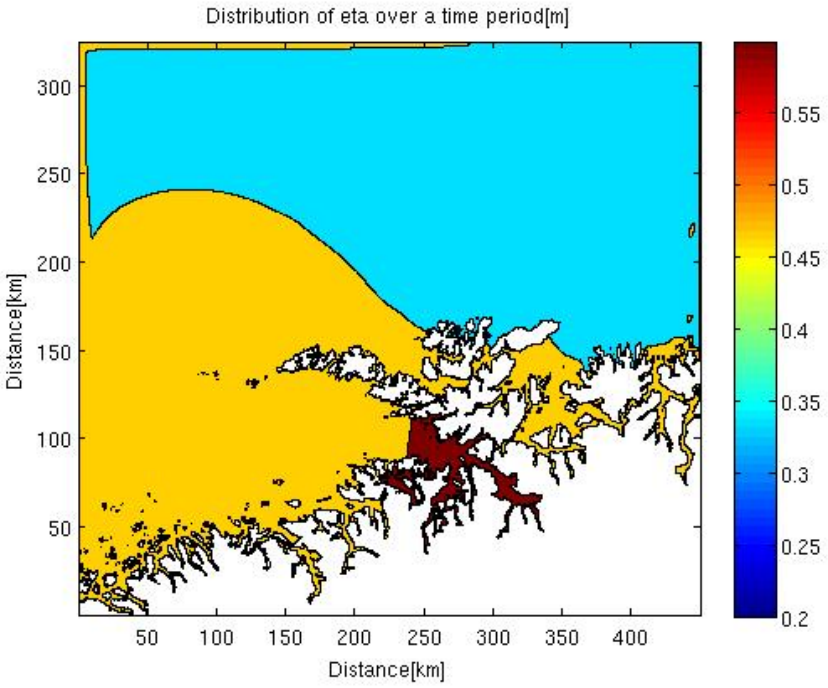

Figure 4.3: The distribution of mean surface elevations for the Lofoten area in meters

The figure shows that the mean surface elevations inside Vestfjorden generally are larger than on the outside of Lofoten. The difference can change from 10 cm some places to almost 30 cm some other places. The surface elevation gradients will force water through the channels and make strong currents there. However, these channels are not large enough to equalize the pressure difference on the outside and the inside of Lofoten. The Lofoten islands appear to make a blocking effect. The volume fluxes through 10 transects in the Lofoten area will be given in Table 4.3 to illustrate this blocking effect. For the explanation of the transects, see

the beginning of the next section about the energy fluxes and the energy losses. The volume fluxes have been computed according to Equation (2.13).

	$A_{M2D} = 0.01\text{m}^2\text{s}^{-1}$			$A_{M2D} = 0.1\text{m}^2\text{s}^{-1}$	$A_{M2D} = 1\text{m}^2\text{s}^{-1}$	$A_{M2D} = 10\text{m}^2\text{s}^{-1}$	$A_{M2D} = 100\text{m}^2\text{s}^{-1}$
	VF	VF	VF	VF	VF	VF	VF
Channel	$1 * 10^5$ m^3s^{-1}						
Saltstraumen	0.0546	0.0534	0.0540	0.0542	0.0549	0.0589	0.0595
Tjeldsundet	0	0.8036	0.0829	0.0830	0.0828	0.0817	0.0575
Raftsundet	0	0.0424	0.0452	0.0452	0.0451	0.0440	0.0278
Gimsøystraumen	0	0.1193	0.1265	0.1265	0.1262	0.1251	0.0991
Grundstadveien	0	0.0409	0.0431	0.0431	0.0429	0.0405	0.0275
Nappstraumen	0	0.1399	0.1476	0.1477	0.1475	0.1467	0.1195
Moskstraumen	2.4798	2.3128	2.4815	2.5050	2.5414	2.4289	2.3444
Værøy-Røst	3.8834	3.4751	3.7357	3.7298	3.7144	3.7384	3.7412
Røst sør	5.2030	4.7247	5.0255	5.0201	5.0109	5.0544	5.1300
Røst vest	2.1716	1.8686	2.0739	2.0722	2.0637	2.0655	2.0719

Table 4.3: Volume fluxes through the transects

The order of the columns are the same as in Table 4.2. The table shows that the volume fluxes are almost not affected and seem to be robust to changes in A_{M2D}. The blocking effect is clearly appearing as the table shows that the volume fluxes almost remain the same independent of channels 2-6 are open or closed. This also explains why the closing of channels 2-6 did not have much effect on the amplitudes in Table 4.2.

When the difference of the surface elevations cannot be equalized by the channels, it must be equalized by something else. The difference of the mean surface elevations can be explained if we understand how the tide behaves. When the tide is propagating towards Lofoten, there will be created a Kelvin wave that propagates along the norwegian coast. When the wave meets the Lofoten islands, it will start to propagate to the inside of the islands into Vestfjorden. This increases the surface elevation towards Narvik which lies innermost in the fjord, see Figure 4.4. The figure shows the behavior of the tide and how the surface elevations are distributed during one tidal cycle. There are 8 plots that are taken from 8 different times within a tidal cycle with equal time between each plot.

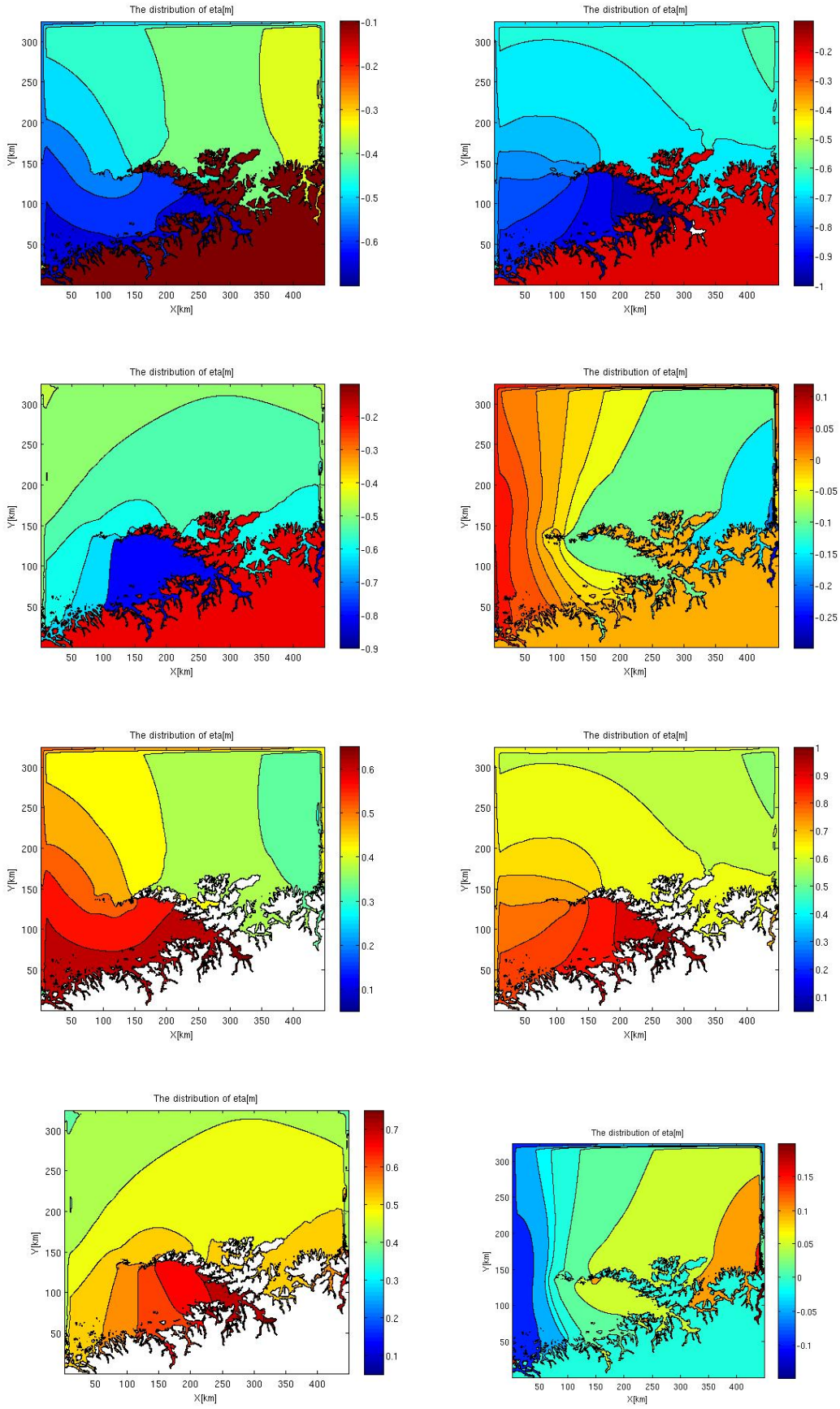

Figure 4.4: The behaviour of the tide during one tidal cycle

The velocity of the currents in the channels will start to increase as Vestfjorden is filled up, but as already mentioned they will not be able to equalize the increasing pressure difference between the inside and outside of the Lofoten islands. The blocking effect creates phase differences between the tide on the outside and the inside and this will force the Kelvin wave to propagate on the outside of Lofoten. After a while the surface elevation between the inside and outside will be more equalized. When the Kelvin wave has passed the Lofoten islands, the water in Vestfjorden will start to flow away and there will again be created pressure differences the opposite way. This will create currents the other way in the channels.

Since some of the water has to move on the outside of Lofoten, one could ask how the situation would be like if all the water was allowed to go through the channels as currents. The following plot shows how the surface elevation is distributed when Tjeldsundet has been made larger as discussed previously.

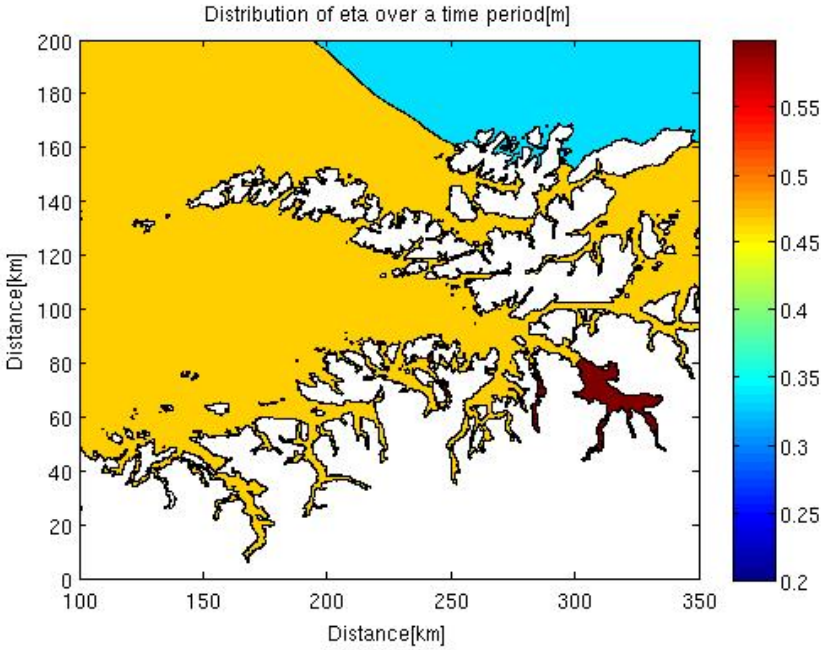

Figure 4.5: The distribution of mean surface elevations when Tjeldsundet is made larger

The figure shows that the red area with the largest mean surface elevations is smaller than in Figure 4.3. The surface elevations are more equalized, which means that much more of the water is allowed to go through Tjeldsundet when the Kelvin wave enters Lofoten. This verifies the results from Table 4.2 which shows that the amplitudes in Vestfjorden have decreased. The volume fluxes in Table 4.3 also verify this result. The table shows that the volume flux

through Tjeldsundet is about 10 times larger than for the other scenarios. This will have an effect on the energy flux which will be discussed in the next section.

4.3 Energy fluxes and energy losses

4.3.1 Energy fluxes

To calculate the energy fluxes, the formulas

$$E_K = \int \frac{1}{2}\rho H|\mathbf{U_H}|^3 dr \tag{4.10}$$

and

$$E_P = \int \rho g H|\eta||\mathbf{U_H}| dr\ , \tag{4.11}$$

as also stated in Chapter 2 have been used. The kinetic energy flux is denoted by E_K while the potential energy flux is denoted by E_P. In the equations, $\mathbf{U_H} = \sqrt{u^2 + v^2}$, H is the depth which is given by the bottom matrix and dr is a small length element across the channel. The other symbols are as described previously. The formulas have units [kgm^{2}s^{-3}=W]. In the channels, the velocity will increase which leads to an increase in both the kinetic and potential energy flux. The depth H in Equations (4.10) and (4.11) will decrease in the channels, but the velocity increases more which gives an increase in total for both the kinetic and potential energy flux. The kinetic energy flux gives how much energy that theoretically can be utilized in the channels, so in some sense this is the quantity of most interest. However, the potential energy flux quantity tells us how much energy that is theoretically available due to differences in the surface elevation for the Lofoten area. As already mentioned, the Kelvin wave was forced on the outside of Lofoten because of the blocking effect. The question that arises is if the topography of the channels could be modified in a more beneficial way to optimize the transfer of potential energy to kinetic energy. That could be to make the channels larger or deeper to equalize the surface elevations between the outside and the inside of Lofoten completely during a tidal cycle. Then the Kelvin wave would not be forced on the outside of the islands. By changing the topography of the channels, more potential energy could be converted to kinetic energy in the channels and more could be utilized.

We notice that the kinetic and potential energy flux in Equation (4.10) and Equation (4.11) always will be positive. This ensures that the flux is positive independent of the direction of the flow. For the discrete case the formulas become

$$E_K = \sum \frac{1}{2}\rho H|\mathbf{U_H}|^3 \Delta x \tag{4.12}$$

and

$$E_P = \sum \rho g H |\mathbf{U_H}||\eta| \Delta x \ . \tag{4.13}$$

The variable Δx is a small length element along a transect which is made across some channel. Time series for the channels have been plotted. An average from the values of each time step in the last tidal cycle has been computed according to

$$\begin{aligned} \overline{E_K} &= \frac{1}{T_{M_2}} \int_{T_{end}-T_{M_2}}^{T_{end}} E_K dt \ , \\ \overline{E_P} &= \frac{1}{T_{M_2}} \int_{T_{end}-T_{M_2}}^{T_{end}} E_P dt \end{aligned} \tag{4.14}$$

to give the average energy fluxes in the channels. In Equation (4.12) and (4.13) it is assumed that the flow will be perpendicular to the channel. This is due to the fact that if a mill was placed in the channel, it would make an angle such that the flow would be perpendicular to the mill. Therefore, the formulas are appropriate for calculating energy fluxes.

The velocity field computed from the model was applied to calculate energy fluxes through 10 transects given in Figure 4.6:

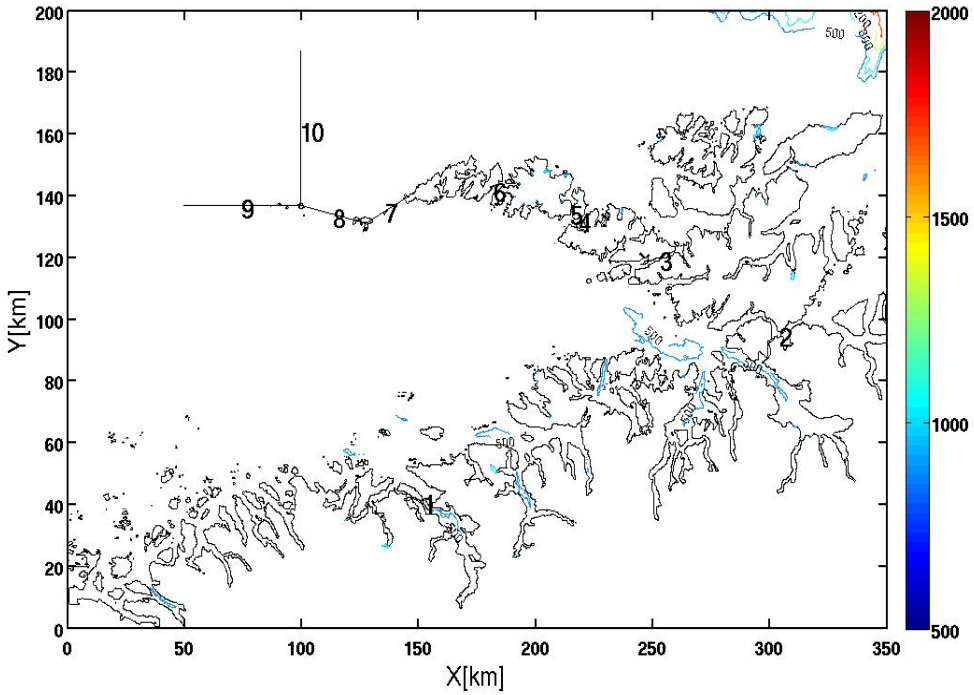

Figure 4.6: The location of the transects

The numbers correspond to the transects. The names and coordinates of the transects in Figure 4.6 are given in the following table:

Number	Place	Coordinates
1	Saltstraumen	(151.25,41.25)-(152.25,41.25)
2	Tjeldsundet	(304.75,94.5)-(304.75,96.25)
3	Raftsundet	(253.75,119.75)-(253.75,120.5)
4	Gimsøystraumen	(219,131.5)-(219,133.25)
5	Grundstadveien	(215,135)-(215.75,135)
6	Nappstraumen	(183.75,141.25)-(181.75,143.25)
7	Moskstraumen	(145,139.75)-(127.5,131.25)
8	Værøy-Røst	(127.5,131.25)-(99.75,136.75)
9	Røst sør	(99.75,136.75)-(49.75,136.75)
10	Røst vest	(99.75,136.75)-(99.75,186.75)

Table 4.4: Name of the transects

The time series for the kinetic and potential energy flux will be shown for Moskstraumen.

The corresponding solutions for the other transects have the same behavior and will not be shown.

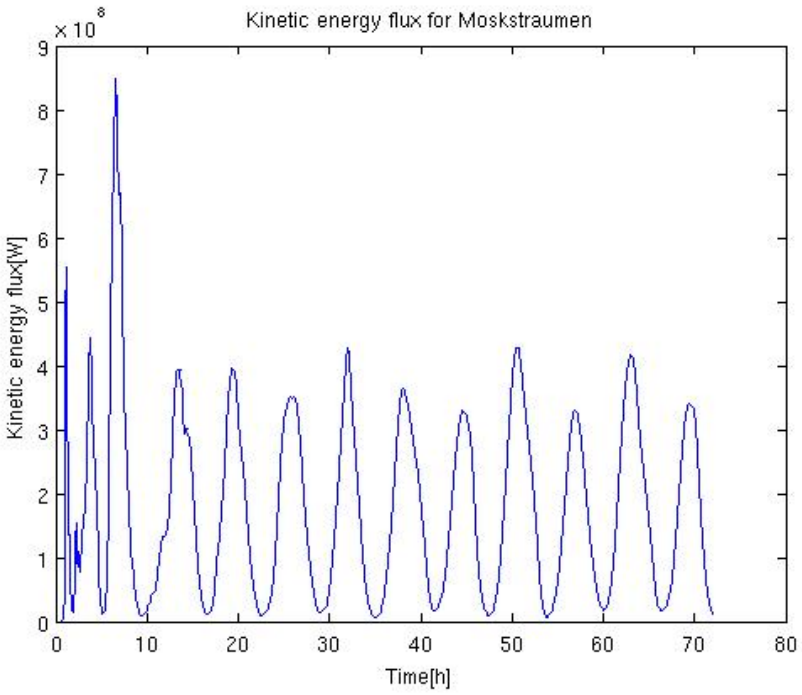

Figure 4.7: Kinetic energy flux in Moskstraumen

The solution is stable and reaches steady state after approximately two tidal periods. When the steady state is reached, the amplitudes for one period are not equal. These changes are due to the direction of the current in the channel. The difference in amplitudes is caused by the topography around and in the inlets. How much of a wave that propagates on the inside or outside depends on the topography and will change depending on the direction for the current. The changes in topography on the east and west side of Moskstraumen give the changes in amplitudes in Figure 4.7.

The potential energy is plotted in Figure 4.8:

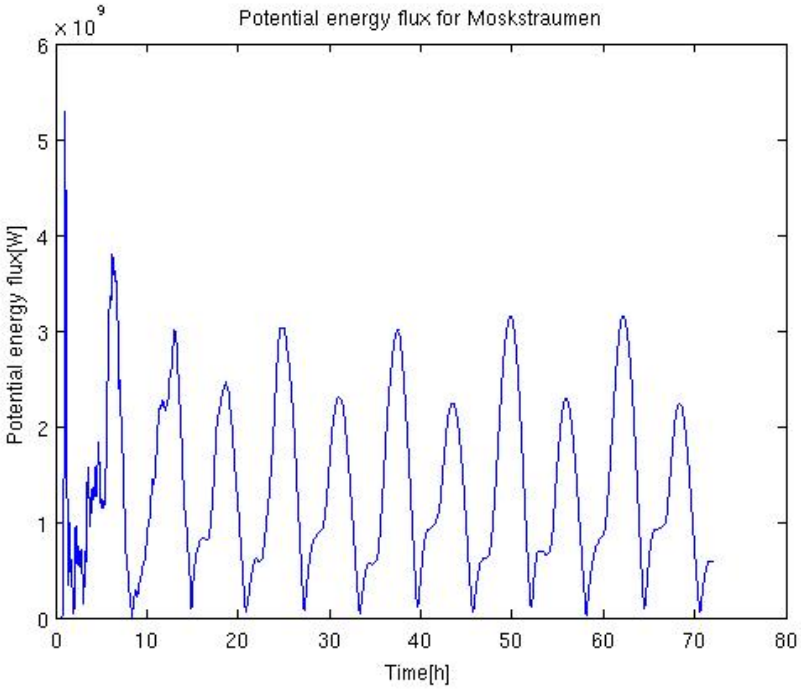

Figure 4.8: Potential energy flux in Moskstraumen

The plot shows that as the potential energy flux increases, small jumps that decreases the flux occurs. As the current flows through the channel, the velocity increases. However, at some point a critical velocity U_{Crit} is reached and due to the topography of the channel, horizontal eddies will be created. This creates separation of water in the channel and some of the energy of the flow will be dissipated. This gives the small jumps in Figure 4.8. The Reynolds number gives an indication of when eddies are created. The Reynolds number is given by $\frac{UL}{A_{M2D}}$ where U and L represent a velocity scale and a length scale respectively. The Reynolds number is dimensionless. Chapter 9 in Kundu see [16] discusses for which values of the Reynolds number, transitions to turbulence are generated. As the velocity scale U increases in our case, the Reynolds number reaches a critical level and the eddies and separations are generated.

The calculation of the energy fluxes through the channels has as mentioned been split into the kinetic and potential energy flux. As shown in Figure 4.7 and Figure 4.8 a transient term affected the solution, but afterwards the solution reached steady state. Therefore the averages of the energy fluxes given in Equation 4.14 were calculated. The results are given in Table 4.5:

	$A_{M2D} = 0.01\text{m}^2\text{s}^{-1}$						$A_{M2D} = 0.1\text{m}^2\text{s}^{-1}$		$A_{M2D} = 1\text{m}^2\text{s}^{-1}$		$A_{M2D} = 10\text{m}^2\text{s}^{-1}$		$A_{M2D} = 100\text{m}^2\text{s}^{-1}$	
	E_K	E_P	E_K	E_P	E_K	E_P	E_K	E_P	E_K	E_P	E_K	E_P	E_K	E_P
Channel	$1*10^9$		$1*10^9$ W		$1*10^9$ W		$1*10^9$ W		$1*10^9$ W		$1*10^9$ W		$1*10^9$ W	
Saltstraumen	0.0006	0.0294	0.0005	0.0282	0.0006	0.0289	0.0006	0.0289	0.0006	0.0288	0.0006	0.0275	0.0005	0.0274
Tjeldsundet	0	0	0.0017	0.4440	0.0030	0.0511	0.0030	0.0512	0.0030	0.0510	0.0026	0.0500	0.0011	0.0371
Raftsundet	0	0	0.0013	0.0263	0.0016	0.0288	0.0016	0.0288	0.0016	0.0287	0.0014	0.0279	0.0003	0.0178
Gimsøystraumen	0	0	0.0051	0.0678	0.0061	0.0738	0.0061	0.0739	0.0061	0.0737	0.0058	0.0733	0.0028	0.0629
Grundstadveien	0	0	0.0005	0.0242	0.0006	0.0259	0.0006	0.0259	0.0006	0.0256	0.0004	0.0235	0.0002	0.0159
Nappstraumen	0	0	0.0021	0.0939	0.0025	0.1014	0.0025	0.1014	0.0024	0.1002	0.0020	0.0966	0.0009	0.0775
Moskstraumen	0.1794	1.4192	0.1391	1.2539	0.1770	1.3943	0.1770	1.4156	0.1790	1.3765	0.1589	1.3443	0.1304	1.2234
Værøy-Røst	0.0755	1.9636	0.0547	1.7224	0.0674	1.8688	0.0673	1.8681	0.0660	1.8568	0.0636	1.8509	0.0529	1.7872
Røst sør	0.0180	2.4355	0.0138	2.1649	0.0163	2.3293	0.0163	2.3266	0.0160	2.3098	0.0157	2.3046	0.0140	2.2801
Røst vest	0.0046	2.5028	0.0036	2.2467	0.0042	2.4149	0.0042	2.4149	0.0042	2.4055	0.0039	2.3955	0.0033	2.3756

Table 4.5: Energy fluxes through the channels

The order of the columns are the same as in Table 4.2 and Table 4.3. For the computations of each value of A_{M2D}, both the kinetic and potential energy fluxes are given. As the eddy viscosity A_{M2D} is increased, Table 4.5 shows that the kinetic and potential energy flux are slightly decreased in the channels, but still the fluxes are quite robust to the changes of A_{M2D}.

The results for $A_{M2D} = 0.01$ m^2s^{-1} show that when channels 2-6 are closed, the kinetic energy flux is slightly increased in the other channels. However, the difference is not large because of the blocking effect. For the other case, when Tjeldsundet has been made larger, the kinetic energy flux decreases in all the other channels. Surprisingly, the kinetic energy flux in Tjeldsundet also decreases. However, we notice that the potential energy flux in Tjeldsundet has become about 10 times larger than for the usual case. When the size of Tjeldsundet is too large, the kinetic energy flux decreases. However, the depth has increased so the speed of the wave $c = \sqrt{gH}$ has increased and therefore the potential energy flux increases. To be able to utilize the energy, we are interested in the kinetic energy flux. However, the ability to convert the potential energy flux over to kinetic energy flux is also very important. The way Tjeldsundet was modified was not optimal for this situation. The question that arises is therefore what width and depth that should be applied to optimize the kinetic energy flux in the channels.

By summing up the energy flux in all the channels for $A_{M2D} = 0.01\text{m}^2\text{s}^{-1}$, we get a total kinetic energy flux of $E_{KTOT} = 2.79 * 10^8$ W and a total potential energy flux at

$E_{PTOT} = 8.32 * 10^9$ W. For one year this gives $E_{KTOT} * 8760h = 2.45 * 10^{12}Wh = 2.45$ TWh and $E_{PTOT} * 8760h = 7.29 * 10^{13}Wh = 72.9$TWh. Grabbe et al. [13] suggests that the kinetic energy flux that theoretically can be utilized in Norway is about 17 TWh per year. The article however, does not include the potential energy flux in the calculations. This thesis shows that the potential energy can give contribution to utilize more than 17 TWh only for the Lofoten area if we were able to convert the potential energy flux to kinetic energy flux. In the report about the potential of ocean energy from ENOVA SF, see [9], it is stated a totally potential of about 1 TWh per year. For this estimate, all the tidal components discussed in Chapter 1 are considered. This is in opposition to our results that only are based on the M_2-component. The estimate is taken from 24 currents where 5 of the currents are the same as also have been calculated in this thesis. These are Saltstraumen, Raftsundet, Moskstraumen, Nappstraumen and Gimsøystraumen. The following table compares the kinetic energy fluxes estimated from our model with the estimates from the ENOVA report.

	Kinetic energy[TWh]	
	Estimate from the model[TWh]	Estimate from the ENOVA report[TWh]
Saltstraumen	0.0053	0.030
Raftsundet	0.014	0.006
Gimsøystraumen	0.053	0.015
Nappstraumen	0.022	0.018
Moskstraumen	1.551	0.758

Table 4.6: Kinetic energy fluxes from this thesis compared with the kinetic energy fluxes from the ENOVA report

Generally, our model estimates larger values for the kinetic energy fluxes than the estimates from the ENOVA report. The ENOVA report has also not included the effect from the potential energy flux. The results from our model show that the magnitude of the potential energy flux makes it very interesting to take this quantity into consideration.

Another interesting investigation was to calculate the energy flux for the whole area on Figure 4.2. This was done by making vertical cross sections for each fortieth grid point in the x-direction. Then the kinetic energy flux and potential energy flux that crossed each cross section were calculated according to Equation (4.12) and Equation (4.13). The situation is depicted in Figure 4.9:

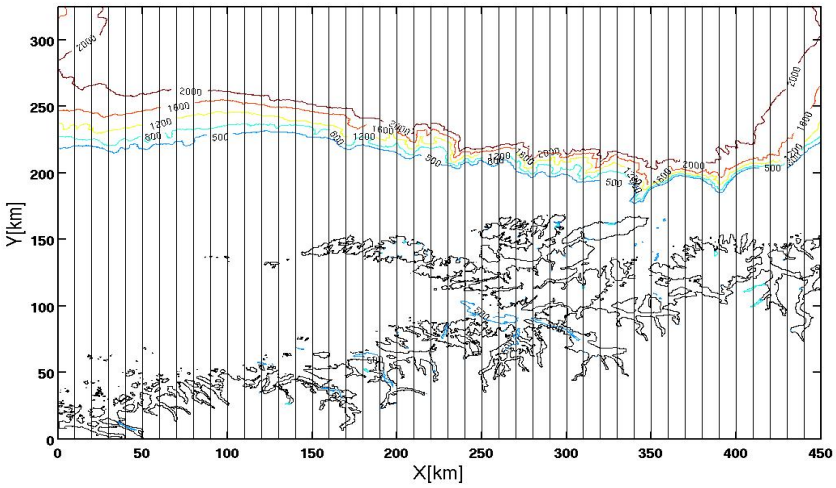

Figure 4.9: Transects for calculating energy fluxes

The fluxes for the last M_2-period were used to calculate an average energy flux for each cross section according to Equation (4.14). The result for how the kinetic energy flux was distributed is given in the following plot:

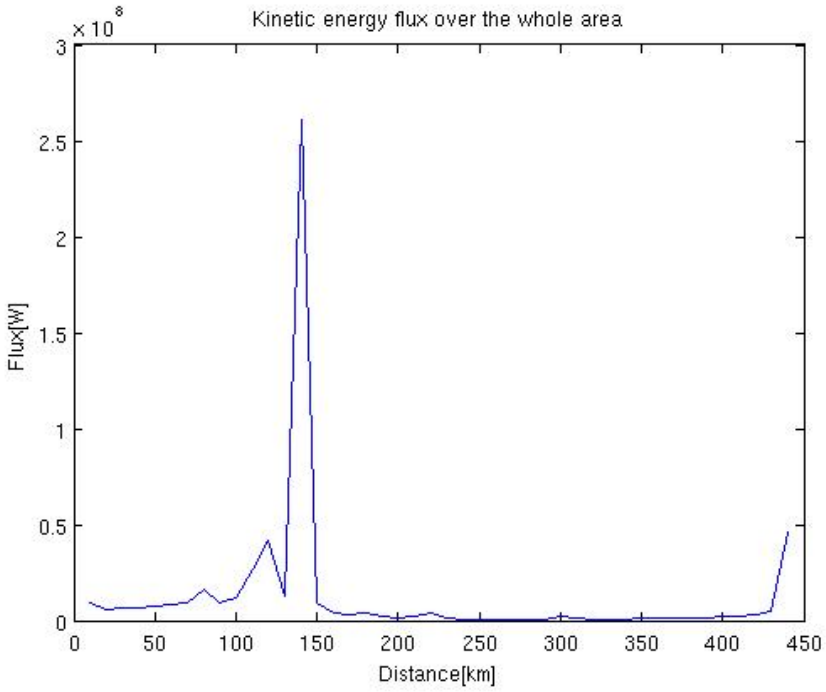

Figure 4.10: Kinetic energy flux for the Lofoten area

The peak occurs in the area around Moskstraumen. The velocity increases in the shallow areas and from Equation (4.12) the kinetic energy flux increases. There is a large shallow area called Røstbanken that affects the flow here. This is in opposition to the other channels where the shallow areas are much smaller and the flow is not significantly affected. The channels can create strong currents, but since these are small they do not affect the kinetic energy flux across an entire cross section.

The potential energy fluxes through the cross sections in Figure 4.9 are given in the following plot:

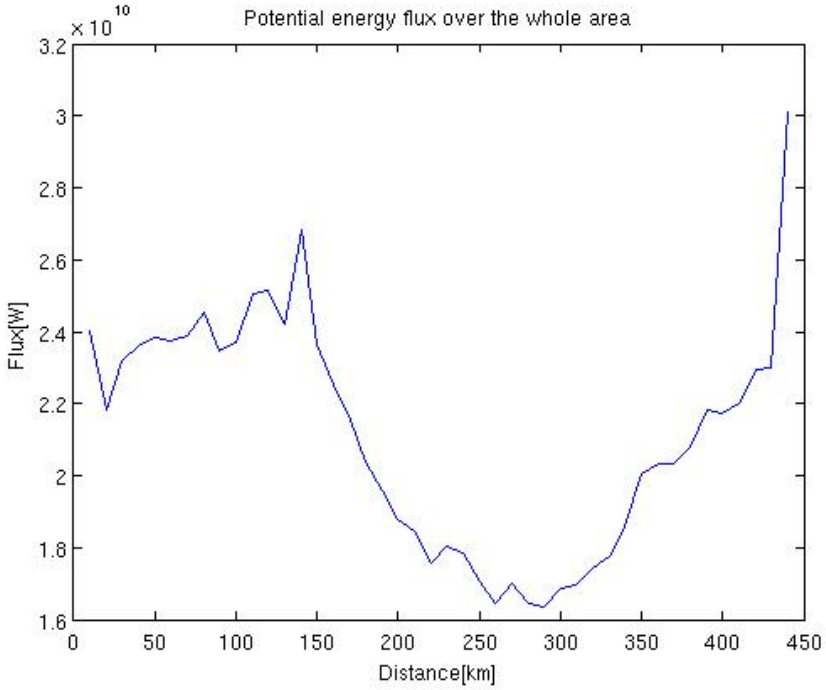

Figure 4.11: Potential energy flux for the Lofoten area

As mentioned earlier in this chapter, the Kelvin wave is forced to propagate on the outside of the Lofoten islands as well as through the channels. When the Kelvin wave propagates around Lofoten, the friction from land causes a decline of the the wave speed. Then there will be a decline in wave speed on both the inside and the outside. This gives a decline in the potential energy flux which is shown in Figure 4.11. When the wave has passed the Lofoten islands, the friction is smaller because there is less land to slow down the wave. The wave is not longer slowed down as before. Then the wave speed increases which again leads to an increase of potential energy. An important fact is that the amount of land is different for the

various cross sections. Therefore the fluxes for the cross sections placed over the Lofoten area will be smaller because there is no flux on land. This is also the reason for the decline of potential energy flux in Figure 4.11.

To estimate the distribution of both kinetic and potential energy for the whole area, the energy fluxes per cross section normal to the flow have been computed in each grid cell. The formulas are the same as in Equation (4.12) and Equation (4.13), except that the flux has not been integrated along a transect.

$$\begin{aligned} E_K &= \frac{1}{2}\rho H|\mathbf{U_H}|^3 \text{ and} \\ E_P &= g\rho H|\mathbf{U_H}||\eta| \ . \end{aligned} \tag{4.15}$$

The units are [Wm^{-1}]. It is expected that the values for the kinetic and potential energy are large in the channels. The following plot illustrates the distribution of the kinetic energy flux for the Lofoten area.

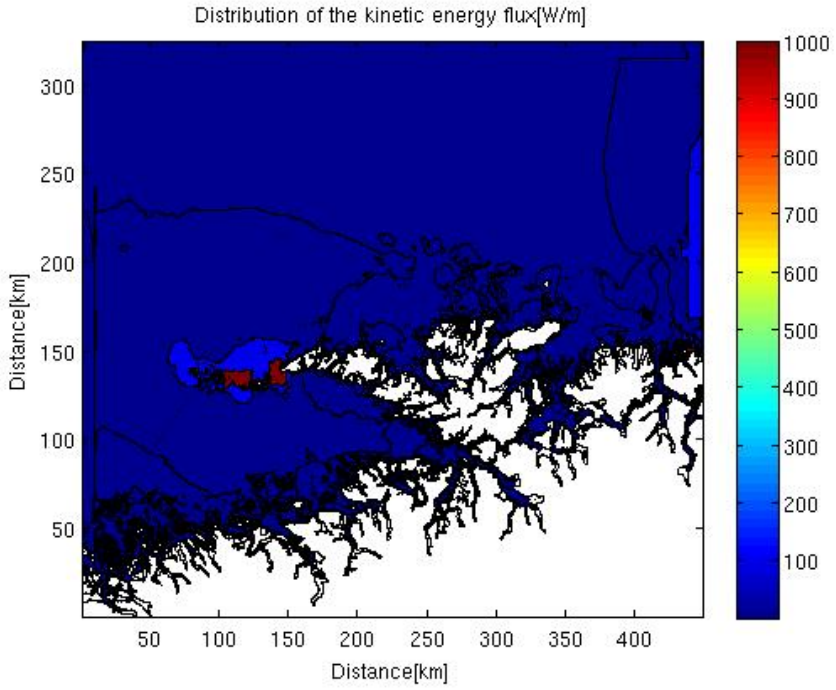

Figure 4.12: Kinetic energy flux for the Lofoten area

The colorbar shows that the dark red area in Moskstraumen has a kinetic energy flux of order 10^3 Wm^{-1}. The figure verifies what also was shown in Figure 4.10. When the current has to move through Moskstraumen, the speed of the current has to increase because of all

the water on the outside that makes a pressure towards the channel. The topography of Moskstraumen allows the current to go straight through it. This is in opposition to many of the other currents in Lofoten where the channels are bent. This gives a loss of the velocity of the current and the kinetic energy flux decreases.

Even though many of the channels in Lofoten can be utilized to exploit energy, Moskstraumen appears to be the area of most interest. The size and location of the channel makes it very beneficial. Among the channels, Moskstraumen is the one that is most suitable for converting the potential energy to kinetic energy. If the other channels were constructed in a more optimal way, an increase of the kinetic energy flux could also be achieved there. Figure 4.11 shows that the potential energy flux is of the order 20 GW which is much more than for the kinetic energy flux which is of order 0.1GW. If we were able to utilize the potential energy, that is converting the potential energy flux to kinetic energy flux, the tidal resource in the Lofoten area could be about 200 times larger. The following plot illustrates an interesting fact:

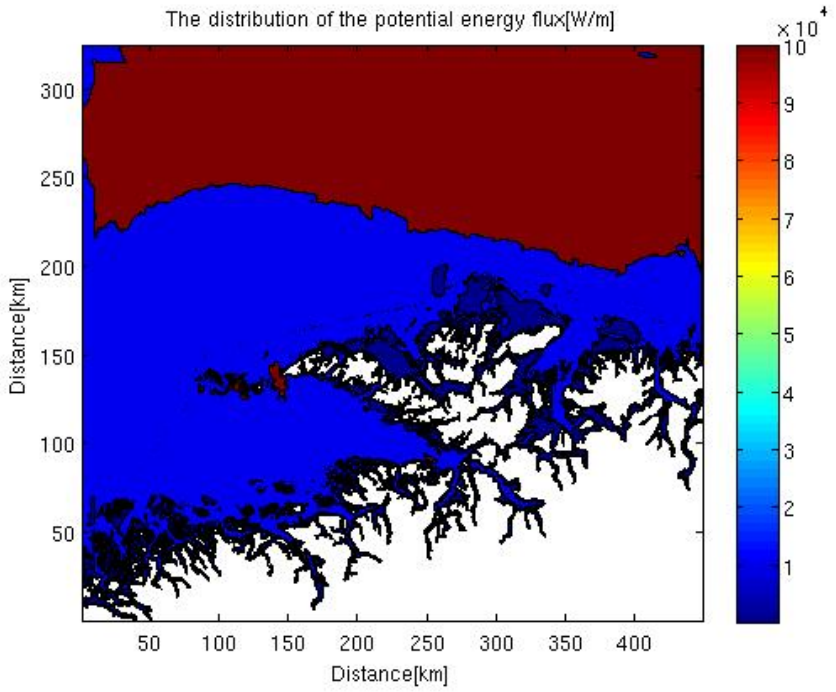

Figure 4.13: Distribution of the potential energy flux

The red area in the deep ocean outside Lofoten shows that there is a large potential energy reservoir that can be utilized. As shown in Figure 4.2 the continental shelf outside Lofoten

is very steep. This causes a separation of two Kelvin waves going in the same direction but with different speed. One that propagates out in the deep ocean and one that propagates along the land boundary (the picture is actually not that idealized. The two fronts of the waves will cause barotropic instabilities but on the large scale we can think that the two waves are separated). The phase speed of a wave is known as $c = \sqrt{gH}$ where g is the gravity acceleration and H is the depth. This shows that when the depth is large, the phase speed gets large. This means that the wave propagating out in the deep ocean has much higher speed than the wave propagating along the land boundary. The formula for the potential energy flux in Equation (4.15) can be written as $E_P = g\rho H|\mathbf{U_H}||\eta| = c^2\rho|\mathbf{U_H}||\eta|$. In the deep ocean, the velocity of the current $\mathbf{U_H}$ is smaller than by the land boundary. However the phase speed is squared so this term is dominating the size of the flux. Therefore there is a large potential energy flux out in the deep ocean.

4.3.2 Energy losses

As mentioned in the introduction chapter in this thesis, some of the energy of the wave will dissipate in both shallow and deep ocean because of the bottom friction and the viscosity. The energy losses per area due to viscosity and bottom friction have therefore been calculated. From Equation (4.8) it follows that the energy loss due to bottom friction can be calculated according to

$$E_{bloss} = -\frac{1}{2}C_D\rho|\mathbf{U_H}|^3 \ , \tag{4.16}$$

with unit [Wm^{-2}]. The energy loss due to viscosity was calculated based on Equation (4.4)-(4.5) to get

$$E_{vloss} = -\sqrt{F_x^2 + F_y^2}\frac{1}{2}\rho|\mathbf{U_H}| \ , \tag{4.17}$$

also with unit [Wm^{-2}]. The expressions for F_x and F_y are given in Equation (4.4)-(4.5). When dealing with these terms numerically, the derivative inside the parentheses has first been solved by finite differences to center it in the spatial grid. Then the constant A_{M2D} has been interpolated to the same point as the derivative according to the Arakawa C-grid. At the end, a finite difference scheme has been used to find the x-derivative and y-derivative respectively for the term inside the parentheses. The results have been used to make contour plots over the distribution of the energy loss for the Lofoten area. It is expected that the areas in and around the channels will give the largest energy loss since these are shallow areas. Then the bottom friction and viscosity will affect the flow more than out on the deep ocean. Therefore the plots that follow are zoomed in to only contain the Lofoten islands.

The magnitude of how much energy that dissipates will be presented next. The solution

for the bottom friction follows in the next plot. The solution is zoomed to the area around Moskstraumen.

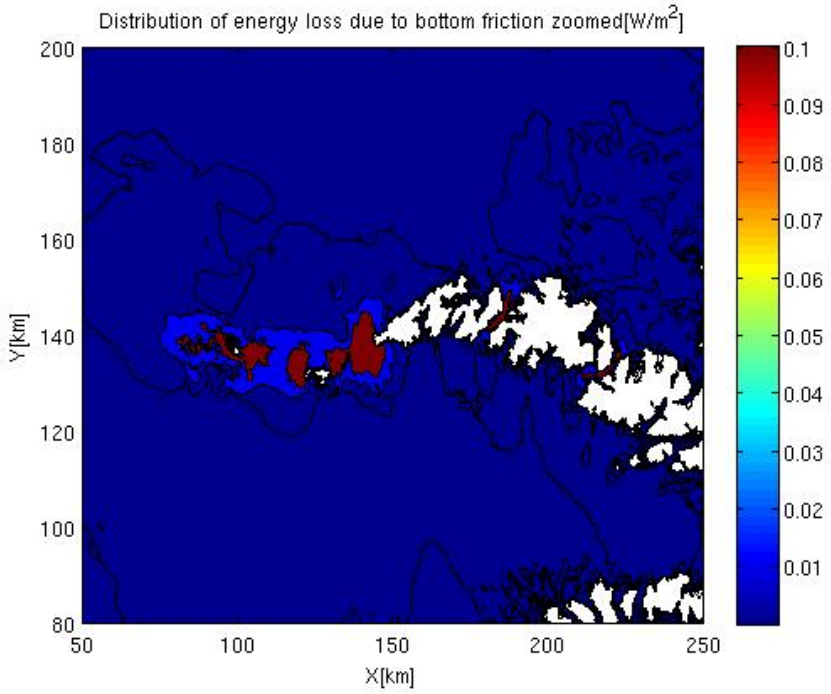

Figure 4.14: Energy loss due to bottom friction

The figure verifies that the main losses occur in the channels. The energy loss in Moskstraumen appears to be of largest magnitude. The magnitude in Moskstraumen is about 0.1 Wm^{-2}.

The energy loss due to viscosity is given next:

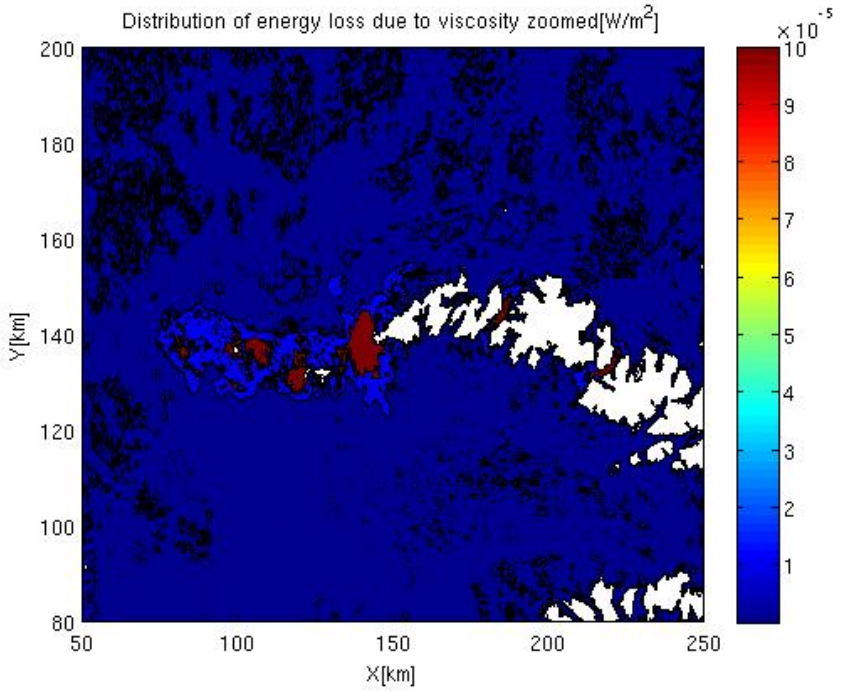

Figure 4.15: Energy loss due to viscosity

The hot spots for energy loss due to viscosity are, as also showed in the figure, located in the channels. This plot is taken from $A_{M2D} = 0.01$ m^{2}s^{-1}. The other plots for the different values of A_{M2D} will give the same behavior, but the magnitudes will increase with almost the same factor as the eddy viscosity.

The total energy loss per square area has been calculated by summing up all the values from the grid cells that were placed in the ocean. The sum for the energy loss due to bottom friction was calculated to be $E_{bloss} = 2.992 * 10^3$ Wm^{-2} and the same loss due to viscosity was calculated to be $E_{\nu loss} = 4.639$ Wm^{-2}. Multiplying the sums over the area gives the energy loss in W. The area used is the size of the grid cells, that is $250 * 250$m^2. This gave a value of $E_{blossarea} = 1.87 * 10^8$ W for our area. The value for the viscosity was computed to be $E_{\nu lossarea} = 2.90 * 10^5$ W. This number is very small compared to the number for the bottom friction. We notice that this number would be much different if another value for the constant A_{M2D} was used. What value of A_{M2D} that is the most correct one is a very difficult question. Because of the uncertainties in this quantity, the bottom friction will be the only quantity discussed further.

It is interesting to see how much of the energy dissipation due to bottom friction that occurs

in the channels compared to the open ocean. A rough estimate of this will be given here. The 8 first channels in Table 4.4 are considered. The last two are not taken into account since they strictly spoken do not represent channels. The area of the channels are roughly estimated by investigating the bottom matrix. The following table shows the x and y grids used for calculating the area of the channels. The last column contains the values for the kinetic energy flux for $A_{M2D} = 0.01$ m^{2}s^{-1} as also given in Table 4.5. This is to compare the magnitudes of the energy dissipation to the kinetic energy flux.

	x-coordinates	y-coordinates	Energy dissipation[W]	Kinetic energy flux[W]
Saltstraumen	605-609	163-168	$2.03 * 10^5$	$0.0006 * 10^9$
Tjeldsundet	1212-1220	378-385	$1.18 * 10^6$	$0.0030 * 10^9$
Raftsundet	1012-1017	479-482	$5.47 * 10^5$	$0.0016 * 10^9$
Gimsøystraumen	871-876	526-533	$1.33 * 10^6$	$0.0061 * 10^9$
Grundstadveien	860-863	536-546	$8.46 * 10^5$	$0.0006 * 10^9$
Nappstraumen	727-735	562-572	$8.48 * 10^5$	$0.0025 * 10^9$
Moskstraumen	510-580	525-559	$6.43 * 10^7$	$0.1770 * 10^9$
Værøy-Røst	399-510	525-547	$1.80 * 10^7$	$0.0674 * 10^9$
Total			$8.73 * 10^7$	$2.59 * 10^8$

Table 4.7: Energy dissipation due to bottom friction

The coordinates in the table represent grid cells. They are not given in kilometers as previously. The table shows that the kinetic energy flux is larger than the energy loss due to bottom friction. By optimizing the topography in the channels, the energy loss could be reduced and the kinetic energy flux could therefore be further increased by a significant amount. The losses from each grid point in the channels were summed to find the total energy loss in the channel. This was multiplied with the area of a grid cell. The table shows that about half of the energy dissipation due to bottom friction occurs in the channels for the Lofoten area. We therefore have an energy dissipation on the open ocean to be $1.87 * 10^8$W-$8.73 * 10^7$W=$9.97 * 10^7$W. Suppose this is the average loss on the open ocean. According to Wikipedia, the area of ocean on earth is about $361 * 10^6$ km^2. By saying that the Lofoten area is $450 * 325$km^2 we get a rough estimate of the total energy dissipation due to bottom friction for the open ocean on the earth to be $2.46 * 10^{11}$W. From Egbert and Ray [7], we saw that the energy dissipation in the open ocean was estimated to be about 1 TW. Our rough estimate is about 4 times smaller than this but as mentioned our estimate does not include the viscosity or the fact that some areas are shallow and some are deep.

Chapter 5

Results for Saltstraumen

What follows in this chapter are the results for the time series in Saltstraumen. With the results from Chapter 3 kept in mind, the results will be discussed further here. The results are given with $A_{M2D} = 0.01$ m^{2}s^{-1} unless anything else is specified.

Figure 4.2 has been zoomed to the area around Saltstraumen. Time series from the model are taken at 9 stations located in the area around Saltstraumen and are also given in the figure. The result was the following:

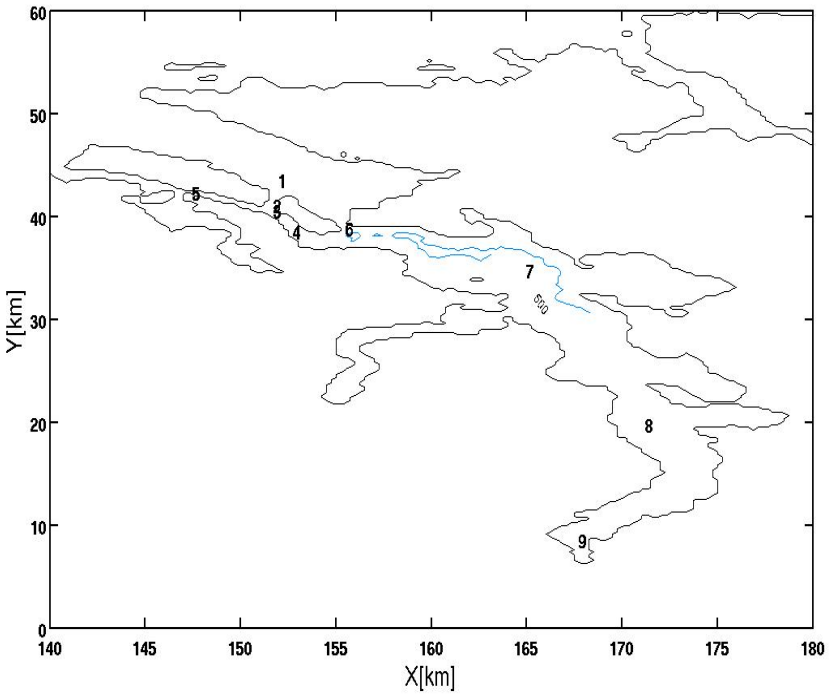

Figure 5.1: The stations where the time series are computed

The numbers 1-9 on the figure are stations where the model has been run. The names and depth of the stations are given in Table 5.1:

Number	Place	Depth[m]
1	The outside	139.1
2	In the current	55.94
3	Inside 1 of the shallow throughflow 1	71.99
4	Inside 2 of the shallow throughflow 2	165.6
5	Sundshavn	5.9
6	Inside Godøystraumen	133.0
7	Skjerstadfjorden 1	431.0
8	Skjerstadfjorden 2	438.8
9	Rognan	57.8

Table 5.1: List over the depth for the stations

As mentioned in Chapter 3 there is a possibility that there can be created seiches in a fjord like Skjerstadfjorden. Therefore the results from Rognan which is the innermost in the

fjord, will be very interesting. The time series will perhaps show small oscillations that can be created due to the local oscillations in Skjerstadfjorden.

When plotting the time series from the model at the stations located in Figure 5.1 and comparing with the solution on the form $\eta_{M2}\sin(\omega_{M2}t)$, a phase delay occurs, see Figure 5.2.

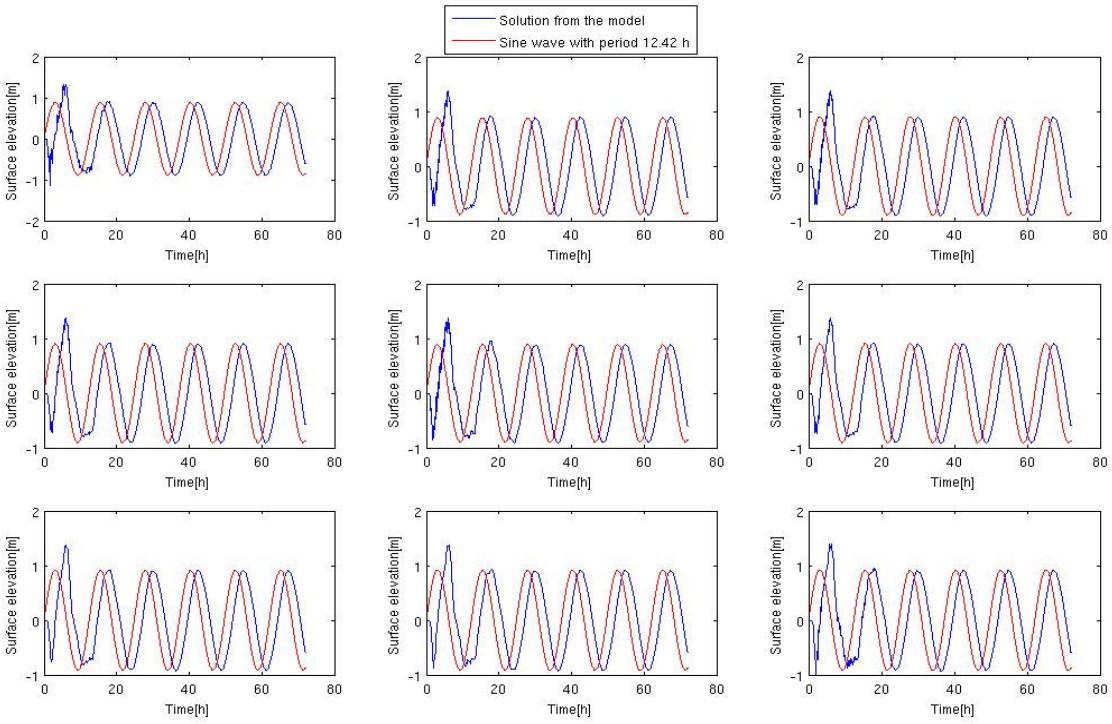

Figure 5.2: Timeseries from the model compared with a sine wave with period T=12.42h

The plots are ordered such that the plots on the first row represent the the solutions of stations 1, 2 and 3. This is in agreement of what was shown in Chapter 3. A simple calculation of the time delays for each station in Figure 5.1 was done in matlab. The procedure for the calculation was the same as briefly described under the section for the quadratic case in Chapter 3 and is given in Table 5.2:

station	1	2	3	4	5	6	7	8	9
time delay[h]	2.15	2.31	2.31	2.28	2.28	2.33	2.29	2.29	2.29

Table 5.2: Time delays for the stations in Figure 5.1 in hours

The time delays reach from 129-140 minutes which are less than what were found in the

calculations for the quadratic drag in Chapter 3.

The phase delays were taken into account, that is, the solutions were modified such that the phase of the solution from the model was the same as the solution from the sine wave. The errors between the solutions from the model and the solution from the sine wave were plotted for stations 7-9 and are given in Figure 5.3.

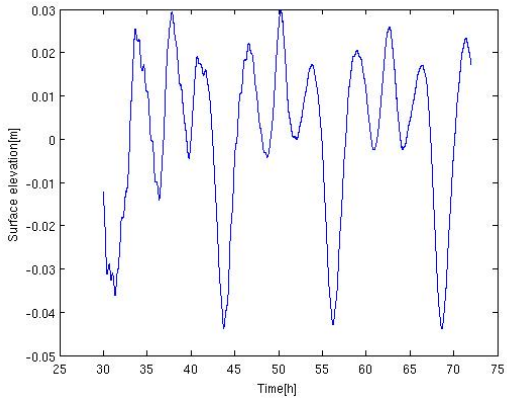

(a) Station 7

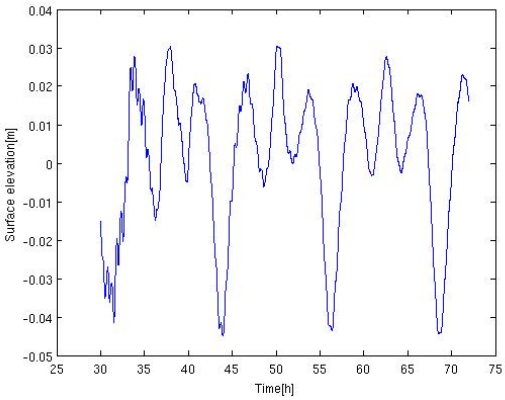

(b) Station 8

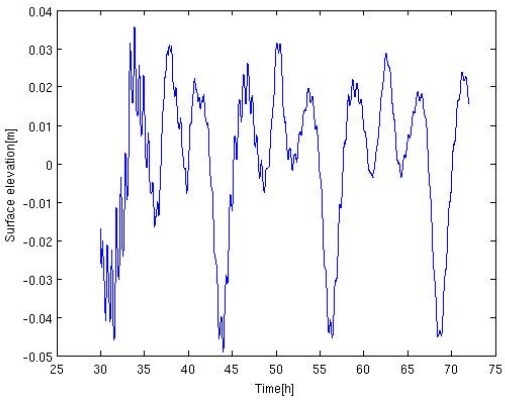

(c) Station 9

Figure 5.3: The error between the sine wave and the solutions from the model

The figures show peaks that occur periodically with a certain time between each peak. The figures suggest that there are some peaks that seem to belong to each other and that the peaks represent different oscillations. Some of these oscillations can be due to higher harmonic modes. The higher harmonic modes occur typically in shallow channels with strong currents and depends much of the topography of the channel. Saltstraumen can be such a place. The higher harmonic modes causes higher harmonic oscillations which have different periods than

the M_2-mode. They are usually referred to as the M_3, M_4, M_6 and M_8-modes which have periods of $\frac{2}{3}$, $\frac{1}{2}$, $\frac{1}{3}$ and $\frac{1}{4}$ of the M_2-period respectively. The best way to investigate which modes that are characteristic for our time series would be to do a FFT(Fast Fourier transformation) to map the time domain over to the frequency domain. However, the time series are too short so this will not be done here. We therefore base our discussion on the plots given in Figure 5.3.

The time series in Figure 5.3 generally behave in the same way and they show that there are some large negative peaks that occur with a period of about 12 hours which is almost the same as the M_2-period. Then there are some positive peaks that seem to occur with a period of about three hours. These peaks can be caused by the higher harmonic modes and this would be an example of the M_8-mode. The plots also show that there are some apparent noise. However, by studying the plots closer these peaks also are periodically oscillations with a period of about 0.5 hours. These peaks also seem to be more visible on the last plot which is the time series for station 9, Rognan. The reason for the peaks is probably the higher harmonic oscillations, but it can also be because of seiches in the fjord as discussed in Chapter 3. This could occur innermost in the fjord by Rognan. From Table 5.1 it is shown that the depth at Rognan is H= 57.8 meters. Using this as the depth and calculating how far the wave will travel during T= 0.5 hours we get $\sqrt{gH} * T = 42.9$ km. By investigating Figure 5.1 it seems reasonable to suggest that the Kelvin wave travels about 40 km on its way from Saltstraumen into Rognan. Thus the two lengths are quite similar which could mean that the small oscillations on the plots represent one of the allowable wavelengths that can occur for a standing wave in Skjerstadfjorden.

Chapter 6

Discussion

During this thesis we have investigated how a box model can be applied to compute the behavior of a tidal flow when a wave comes into a channel that ends up in a bigger basin. The results from this approach were also verified by another numerical model. The computations from the numerical model have shown how the tide behaves around the Lofoten area and a calculation of available kinetic and potential energy fluxes for the Lofoten area has been computed. Energy losses due to bottom friction and viscosity have also been investigated.

6.1 Major results

For the study of available tidal energy in the Lofoten area, the most important results shown in this thesis are:

- The large reservoir of potential energy compared to kinetic energy in both shallow and deep areas
- There is a substantial conversion from potential energy to kinetic energy as the tide enters the channels
- The blocking effect of the Lofoten islands forces the Kelvin wave outside the islands
- The throughflows may be optimized with respect to total energy production

To extend the work from Grabbe et al. [13] and the ENOVA report [9], we investigated the potential energy in the Lofoten area as well as the kinetic energy. We showed that the magnitude of potential energy flux was about 200 times larger than the magnitude of the kinetic energy flux and that this quantity is very important to take into consideration when

we are talking about tidal energy in the Lofoten area. We stated that due to the steep continental shelf, there are two separated Kelvin waves propagating with different wave speeds. The Kelvin wave in the deep ocean traveled faster than the one close to land, representing a large potential energy reservoir in the deep ocean.

As waves with wavelengths of a large scale in the ocean is forced through inlets where waves with wavelengths of a much smaller scale can occur, we saw that this gave a large conversion of the potential energy in the ocean to kinetic energy in the channels. In the channels the velocity of the current increases which leads to an increase of kinetic energy flux. Because the channels are shallow, the wave speed decreases which leads to a decrease of potential energy flux.

We stated that the Lofoten islands made a blocking effect and forced the Kelvin wave to propagate on the outside of the islands. The results showed that Vestfjorden was filled up due to the blocking effect. The islands therefore created large phase differences of the tide on the inside and the outside. The experiment by closing some of the channels showed that the volume fluxes and the amplitudes did almost not change. This also verified the blocking effect. The results also showed that the energy fluxes in the channels were almost not affected by this experiment.

The results when Tjeldsundet was made larger showed that the volume fluxes increased in this channel. We also verified that the phase differences between the inside and the outside of the islands were smaller for this scenario. Furthermore, the potential energy flux increased, but the kinetic energy flux decreased for this scenario. We stated that Tjeldsundet was not optimally modified to achieve maximum conversion of potential energy to kinetic energy.

An important result regarding Saltstraumen was the occurence of the high frequent oscillations in Rognan. The oscillations could represent local seiches that slightly reinforced the amplitude of the tide. In Chapter 3 we showed that oscillations due to seiches can affect the tide when drag is neglected. However, the results in Chapter 5 showed that these oscillations can also occur when the bottom friction is included, but after some time these oscillations will die out.

6.2 Remarks about the model

The dissipation of energy according to bottom friction and viscosity was computed and gave an indication of the energy loss in the earth moon system that was compared to the result given in Egbert and Ray [7]. However, dissipation due to eddies was not taken into account in these calculations. From Figure 4.8, we noticed the small jumps in the solution that occurred due to horizontal eddies created in the channel because of the topography. These eddies were of such a length scale that they were represented by the model. The resolution of the grid applied in the model had as stated a length $\Delta x = \Delta y = 250$ m between each grid point. Thus, an eddy should have longer length scales than $2 * 250 = 500$ meters to be represented by the model, see Haidvogel and Beckmann [14].

If stratification is taken into account the flow can be interpreted as a flow consisting of several layers with different densities. This creates the occurrence of internal waves. Internal waves are small waves created between the layers with different density. By including stratification, pressure gradients will force water to flow in the vertical direction. If a water parcel with high density was placed in a fluid with low density, the water parcel would seek equilibrium and sink towards the fluid with heavier density. In [6] it is described how the water parcels behave when they are placed in a fluid layer with different density. As the water parcel has sunk to the density of equilibrium, the velocity of the parcel is not zero. This means the water parcel will continue to sink to the fluid with higher density than itself. This will make the water parcel to go upwards again. When seeking equilibrium, the water parcel oscillates in the fluid like a wave. These waves are referred to as internal waves and the oscillation just mentioned is referred to as the stratification frequency, also called the Brunt-Vaisala frequency. The viscosity in the internal waves makes energy to dissipate as water parcels with different densities are mixed together. The internal waves can have length scales both long enough but also too short to be resolved by our model.

For even shorter length scales instabilities can still occur. In the channels, the velocity of the current will be smaller in the layers close to the bottom because of the friction. As the topography in the channels changes, there can be created instabilities in the form of eddies on the interface between the layers that drains kinetic energy from the flow. These instabilities are often referred to as Kelvin-Helmholtz instabilities, see Kundu [16]. The eddies created can be of such a small length scale that the model does not resolve them. The kinetic energy loss associated to these instabilities is therefore not considered. However, as discussed earlier in Chapter 4 the choice of A_{M2D} is often chosen to take care of this, but to quantify the loss

is very difficult which means that the choice of A_{M2D} is an uncertain choice.

6.3 Further work

In order to extend the results from this thesis, the following scenarios should be investigated:

- The model should include the tidal components S_2, N_2 and K_1.
- The grid resolution could be improved
- Stratification should be taken into account.
- An estimate of the optimal size of the channels to achieve the optimal transfer of potential energy to kinetic energy should be computed.
- An estimate of the phase delay and the actual energy fluxes as water mills are placed in the channels.

To estimate the results including the other tidal components would be the main research to get a realistic study as possible.

We mentioned in the previous section that energy losses at small scales were not resolved by our model. By refining the grid resolution, these losses would be included. However, suppose $\Delta x = \Delta y = 1$ meter. The large conversion of potential energy on the large scale to kinetic energy on the small scale would be represented even better with this grid resolution. With this resolution the model will estimate larger kinetic energy fluxes in the channels. The inclusion of stratification showed that energy losses due to internal waves and Kelvin-Helmholtz instabilities occur. This will give a smaller estimate for the kinetic energy fluxes. We end up with two arguments that contradict each other. In order to investigate if this will lead to a total increase in kinetic energy flux, focused studies for each throughflow should be computed.

The experiment when Tjeldsundet was made larger should be extended to find the optimal transfer of potential energy to kinetic energy in the channels. To make a channel narrower would increase the energy flux, but at some point the friction in the channel would dominate such that the energy flux would start to decrease. Identification of the optimal size should therefore be an interesting task for the further work.

Appendix A: Symbols

A.1 Symbols used in the modified version of BOM

$\mathbf{U_H} = [u, v]$	Horizontal velocity field [ms^{-1}]
$\mathbf{U} = [u, v, w]$	Velocity field [ms^{-1}]
$\bar{\mathbf{U}}$	Mean velocity field [ms^{-1}]
$\mathbf{U_f}$	Velocity fluctuation [ms^{-1}]
ρ	Density[kgm^{-3}]
ρ_0	Reference density[kgm^{-3}]
ρ'	Density perturbation[kgm^{-3}]
$\eta(x, y, t)$	Surface elevation [m]
$h(x, y, t)$	Dynamic depth [m]
$H(x, y)$	Static depth [m]
$\nabla = \frac{\partial}{\partial x}\mathbf{i} + \frac{\partial}{\partial y}\mathbf{j} + \frac{\partial}{\partial z}\mathbf{k}$	Differential operator
$\mathbf{p}$	pressure [Pa=kgm^{-1}s^{-2}]
$\mathbf{\Omega}$	Earth rotation [rads-1]
$\mathbf{g}$	gravity acceleration[ms^{-2}]
$\mathbf{F} = [F_x, F_y]$	External forces [ms^{-2}]
ϕ	Latitude[rad]
f	Coriolis parameter [s^{-1}]
f_*	Reciprocal Coriolis parameter[s^{-1}]
$\frac{D}{Dt}() = \frac{\partial}{\partial t}() + \mathbf{U}\cdot\nabla()$	Total derivative
$[\mathbf{i}, \mathbf{j}, \mathbf{k}]$	Unit vectors in x,y and z-direction
$c = \sqrt{gH}$	Phase speed[ms^{-1}]
A_{M2D}	Eddy viscosity[m^{2}s^{-1}]
C_M	Smagorinsky constant[1]
$\boldsymbol{\tau_b} = [\tau_{bx}, \tau_{by}]$	Bottom stress[Pa=kgm^{-1}s^{-2}]
Φ_{int}	Unrelaxed value from model
Φ_{ext}	Specified external value in boundary zone
E_P	Potential energy flux[W=kgm^{2}s^{-3}]
E_K	Kinetic energy flux[W=kgm^{2}s^{-3}]

C_D	Drag coefficient[1]
E_{bloss}	Energy loss due to bottom friction[Wm^{-2}=kgs^{-3}]
$E_{\nu loss}$	Energy loss due to viscosity[Wm^{-2}=kgs^{-3}]
η_{M_2}	Semi-diurnal tidal amplitude [m]
T_{M_2}	Main semi-diurnal period [s]
$\omega_{M_2} = \frac{2\pi}{T_{M_2}}$	Semi-diurnal tidal frequency [$rads^{-1}$]
t	Time[s]

A.2 Symbols used in Chapter 3

η_1	Surface elevation in the ocean[m]
η_2	Surface elevation in the fjord[m]
η_3	Surface elevation in the fjord[m]
U_C	Velocity in the channel[ms^{-1}]
U_M	Velocity in the fjord[ms^{-1}]
W_C	Width of channel [m]
H_C	Depth of channel [m]
L_C	Length of channel [m]
L_F	Length of the fjord [m]
A_C	Cross sectional area of channel [m^2]
A_F	Cross sectional area of the fjord[m^2]
A_2	Surface area of fjord[m^2]
R	Friction coefficient [s^{-1}] or [m^{-1}]

Appendix B: Stability of the trapezoidal method

To investigate the stability of a difference scheme, the von-Neumann analysis is often applied. During this thesis the trapezoidal rule has been applied on a system of equations that typically look like:

$$\frac{d}{dt}\begin{bmatrix} \eta_2 \\ U_C \end{bmatrix} = \begin{bmatrix} 0 & -K \\ C & 0 \end{bmatrix}\begin{bmatrix} \eta_2 \\ U_C \end{bmatrix} \tag{1}$$

This problem can be rewritten by vector notation to get:

$$\frac{d}{dt}\boldsymbol{\eta} = i\boldsymbol{\omega}\boldsymbol{\eta} = \mathbf{0}\,.$$

Here $\boldsymbol{\omega}$ denotes a matrix with the eigenvalues of the matrix in (1) on the diagonal and $\boldsymbol{\eta}$ denotes a vector. This problem is the typical test problem and stability is discussed in Haidvogel and Beckmann, see [14]. The discretization gives

$$\boldsymbol{\eta}^{n+1} - \boldsymbol{\eta}^{n} = i\boldsymbol{\omega}\Delta t\frac{1}{2}(\boldsymbol{\eta}^{n} + \boldsymbol{\eta}^{n+1})$$

which gives

$$\boldsymbol{\eta}^{n+1} = \left(\frac{1 + i\frac{1}{2}\boldsymbol{\omega}\Delta t}{1 - i\frac{1}{2}\boldsymbol{\omega}\Delta t}\right)\boldsymbol{\eta}^{n}.$$

The amplification factor, that is, the absolute value of what is inside the parentheses is 1. This gives us that the trapezoidal method is a stable and neutral method, that is no growth and no damping, the method is constant with the properties of the underlying problem.

Bibliography

[1] Robert A. Adams and Christopher Essex. *Calculus A complete course*. Pearson Education Canada, 7th edition, 2010.

[2] Alfatih Ali, Øyvind Thiem, and Jarle Berntsen. Numerical modelling of organic waste dispersion from fjord located fish farms. *Ocean Dynamics*, 61(7):977–989, 2011.

[3] Knut Barthel. Compendium in the course GEOF211: On TVD schemes. 2013.

[4] Jarle Berntsen. Users guide for a modesplit σ-coordinate numerical ocean model version 1.0. 2000.

[5] William E. Boyce and Richard C. DiPrima. *Elementary differential equations and boundary value problems*. John Wiley and Sons, Inc, 9th edition, 2010.

[6] B. Cushman-Roisin and J. M. Beckers. *Introduction to geophysical fluid dynamics, Physical and numerical aspects*. AP, 2nd edition, 2011.

[7] Gary D. Egbert and Richard D. Ray. Estimates of M2 tidal energy dissipation from topex/poseidon altimeter data. *Journal of Geophysical Research: Oceans (1978–2012)*, 106(C10):22475–22502, 2001.

[8] Inge K Eliassen, Yngve Heggelund, and Magne Haakstad. A numerical study of the circulation in saltfjorden, saltstraumen and skjerstadfjorden. *Continental Shelf Research*, 21(15):1669–1689, 2001.

[9] SF Enova. Potensialstudie av havenergi i Norge. 2007.

[10] Chris Garrett and Eric Kunze. Internal tide generation in the deep ocean. *Annu. Rev. Fluid Mech.*, 39:57–87, 2007.

[11] Christopher Garrett. Tides in gulfs. pages 23–35, 1974.

[12] Bjørn Gjevik. *Flo og fjære langs kysten av Norge og Svalbard*. Farleia forlag, 2009.

[13] Mårten Grabbe, Emilia Lalander, Staffan Lundin, and Mats Leijon. A review of the tidal current energy resource in norway. *Renewable and Sustainable Energy Reviews*, 13(8):1898–1909, 2009.

[14] Dale B. Haidvogel and Aike Beckmann. *Numerical ocean circulation modeling.* Imperial college press, 2nd edition, 1999.

[15] Farago Istvan. Splitting method. 2003.

[16] P.K Kundu, I.M Cohen, and D.R Dowling. *Fluid mechanics.* Academic press, 5th edition, 2012.

[17] Eivind A Martinsen and Harald Engedahl. Implementation and testing of a lateral boundary scheme as an open boundary condition in a barotropic ocean model. *Coastal engineering*, 11(5):603–627, 1987.

[18] Halvard Moe, Atle Ommundsen, and Bjørn Gjevik. A high resolution tidal model for the area around the lofoten islands, northern norway. *Continental Shelf Research*, 22(3):485–504, 2002.

[19] Joseph Smagorinsky. General circulation experiments with the primitive equations: I. the basic experiment*. *Monthly weather review*, 91(3):99–164, 1963.

[20] Peter K Sweby. High resolution schemes using flux limiters for hyperbolic conservation laws. *SIAM journal on numerical analysis*, 21(5):995–1011, 1984.

[21] L. Sælen. Lecture notes in ENERGI 200-Energy resources and consumption. Universitetet i Bergen, 2012.